Observations of the Flow of a Semi-Dilute Fibre Suspension Through a Sudden Expansion Using Positron Emission Tomography

by

Stuart James Heath

B.A.Sc., The University of British Columbia, 2003

A THESIS SUBMITTED IN PARTIAL FULFILLMENT OF

THE REQUIREMENTS FOR THE DEGREE OF

Master of Applied Science

in

THE FACULTY OF GRADUATE STUDIES

(MECHANICAL ENGINEERING)

The University of British Columbia

August 2006

Abstract

The motion of ^{18}F radioactively labeled papermaking fibres flowing through an axisymmetric 1:5 sudden expansion has been studied using positron emission tomography (PET). Various length fractions of a mechanical pulp were radioactively labeled and then introduced into a non-radioactive aqueous 0.4 wt. % (consistency) wood pulp suspension. Fully three-dimensional images were reconstructed both upstream and downstream of the expansion plane for cases in which the upstream velocity U was set from 0.5 to 0.9 m/s (an approximate Reynolds number range of 7,000 to 13,000). Two distinct flow regimes were clearly identified. With $U \sim 0.5\,m/s$ we find that the fibre suspension was not fluidized and the tracer fibres passed through the expansion as a plug. No mixing was observed between the confined central jet and the static outer region. At larger velocities, we observed that the suspension was fully fluidized. Our results in this regime indicate that albeit fluidized, concentration inhomogeneities were evident. We find that a particle depletion zone was evident between the central jet and the recirculating zone resulting from the inlet concentration profile formed in the upstream tube. Particle accumulation was observed in the vortices. No significant differences were observed between the different length tracer fibres.

Contents

List of Tables

List of Figures

Acknowledgements

I would like to thank Ken Buckley, Suzy Lapi, and Thomas Ruth from the TRIUMF Life Sciences program for all their hard work, my supervisors Mark Martinez and James Olson for their guidance and insight, and all my friends at the Pulp and Paper Centre. Financial support from the Natural Sciences and Engineering Research Council of Canada and the TRIUMF Life Sciences program are gratefully acknowledged.

STUART JAMES HEATH

The University of British Columbia

August 2006

To my family, Robert, Marie-Claude, Alexandre, and Nathalie for all their support and encouragement.

Chapter 1

Introduction

The focus of the present work is an experimental study of the concentration distribution of a semi-dilute fibre suspension-undergoing steady flow in an abrupt 1:5 sudden expansion. Although the flow of multiphase fluids through sudden expansions is found in many industrial and natural settings, there are still many unanswered questions regarding the mechanism of particle dispersion (fluidization) or clumping (flocculation). The motivation for the present work stems from an interest in the papermaking process. Under normal processing conditions, papermaking suspensions mechanically entangle to form a network, which possesses a measurable yield stress (Duffy & Titchener (1975), Thalen & Wahren (1964a,b)). During processing the suspension is fluidized into individual flocs or fibres, with weakly correlated velocities, by turbulence created locally by an abrupt expansion. This aids in evenly dispersing the suspension. In a paper machine sudden expansions are found in the cross-flow distributor, the turbulence generator, and the headbox nozzle. Suspensions which are evenly dispersed reduce the cloudiness or graininess of the sheet and

aid in the elimination of grammage (areal density) variations, a property that is important for all paper grades. While the objectives of the papermaking process are clear, and the equipment on the paper machine well known, the exact mechanism by which fluidization and material redistribution occurs remains obscure. Our objective is to provide insight into this phenomenon by visualizing the flow of the papermaking suspension through a sudden expansion using Positron Emission Tomography (PET).

Understanding the motion of an aqueous fibre suspension flowing through a sudden expansion is difficult. Insight into this phenomena can be gained by first examining the simpler case of the flow of single-phase fluid. For Newtonian fluids, Macagno & Hung (1967) indicate that over all Reynolds numbers, a vortex exists immediately downstream of the expansion. There is general agreement that at low Re the size of the vortex increases linearly with Reynolds number and then decreases with $Re > 635$ (Latornell & Pollard (1986)) . In contrast with this, Non-Newtonian fluids exhibit vortex lengths that differ significantly from Newtonian fluids. With yield stress fluids, the recirculation lengths were found to be smaller when compared to Newtonian fluids at a comparable Reynolds number (Hammad et al (1999), Jossic et al (2002)).

The case of expansion flows with particle suspensions remains largely unexplored. This class of flow is strikingly different than single-phase flows as particle concentration inhomogeneities are generated through particle collisions, shear induced particle migration (Leighton & Acrivos (1987), Phillips et al (1992)), density differences between the particles and the carrier fluid, inertia; and, in the case of papermaking fibres, mechanical flocculation of the particles fibres (Kerekes et al (1985)). To help illustrate this complexity, there is evidence that with suspensions of neutrally buoyant monodisperse spheres, particle accumulation or depletion is evident in the vortex depending upon the ratio of the upstream

tube to particle diameters (Altobelli et al (1997a,b), Karino & Goldsmith (1977)). In a recent study, Moraczewski et al (2005) observe that a low concentration region exists which divides the central jet and the recirculation region. They attribute this to inhomogeneities in the inlet concentration that were convected downstream. The concentration profiles in this case were measured using NMR after the flow had been stopped.

With regards to papermaking suspensions, there is evidence of seemingly two different behaviours. Arola et al (1998), for example, imaged the axial velocity profile of a 0.5% (wt) wood pulp suspension flowing through a 1:1.7 sudden expansion using nuclear magnetic resonance imaging (NMR). These authors report that the pulp suspension exhibited behavior similar to that of a confined jet. In recent work, Salmela & Kataja (2005) used an optical technique to measure the floc size and fibre flow field of a semi-dilute suspension after the expansion. They report that the recirculation eddy downstream of the expansion plane was found only to exist when the step height exceeds the mean fibre length. When existing, the suspension was fluidized and behaved as a Newtonian fluid.

Our work is focused on complimenting these previous studies by measuring the steady-state concentration profiles of papermaking fibres as they pass through a sudden expansion. Here, the behaviour of Fluorine-18 (^{18}F) labeled papermaking fibres flowing in the midst of non-radioactive fibres are studied using PET. We measure the radioactivity distribution, three-dimensionally, near the expansion plane and then far downstream of the expansion plane. The experimental conditions were such that the bulk concentration of the suspension was fixed while we varied the volumetric flowrate and size of the ^{18}F labeled fibres. The key advantage of this measurement technique is that the concentration profile can be determined for each particle fraction directly without stopping the flow. In addition, we measure the axial velocity of the suspension far downstream of the expansion plane using

pulsed ultrasound Doppler anemometry (UDV).

In chapter 2 the technique behind PET is quickly reviewed. Chapter 3 describes the experimental apparatus and experimental protocol used in this work. The results from the six successful scans are discussed in chapter 4. The results are presented in three subsections. First the effect of velocity is examined, followed by the effect of particle size; and, finally, the observations made far downstream of the expansion. Chapter 5 summarizes the major findings in this work. Appendix A provides a more detailed look at the mathematics of PET; specifically, the filtered-backprojection algorithm used to reconstruct all of the images in this study. Appendix B provides each of the 63 2D slices and associated figures for each of the cases examined in this study.

Chapter 2

Positron Emission Tomography

Positron emission tomography (PET) is a non-invasive imaging technique developed in the medical field for measuring the metabolic activity of cells *in-vivo*. PET is unique because it produces images of basic biochemistry or function, rather than other diagnostic imaging techniques such as x-rays, CT scans or magnetic resonance imaging (MRI), which produce images of anatomy or structure (Ollinger & Fessler (1997)). Positron emitting isotopes of carbon (^{11}C), nitrogen (^{13}N), oxygen (^{15}O) and fluorine (^{18}F) are produced in an on-cite cyclotron and are incorporated into compounds of biological interest. These isotopes have relatively short half-lives of 20.3 minutes, 9.97 minutes, 2.03 minutes and 109.8 minutes respectively. A PET study begins with the injection of a radiopharmaceutical. To allow for transport to, and uptake by, the organ of interest the scan is begun after a delay ranging from seconds to minutes. When the radio-isotope decays it emits a positron, which travels a short distance before annihilating with an electron. This annihilation produces two high-energy (511 keV) photons propagating in nearly opposite directions. If two photons are

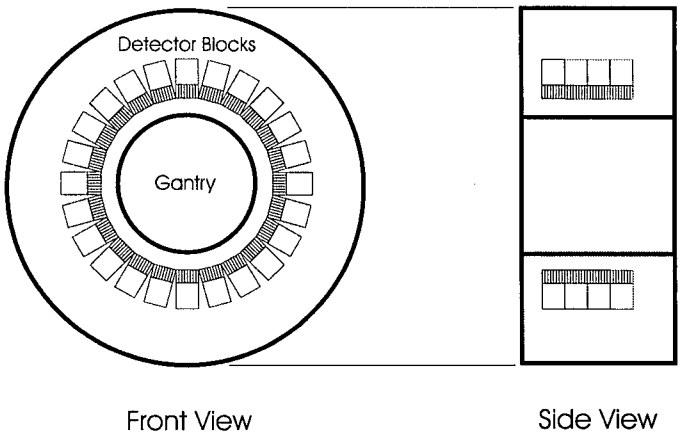

Figure 2.1: Schematic of the detector arrangement in a PET tomograph.

detected in a short ($\sim$10 ns) timing window, an event is recorded along the line connecting the two detectors, sometime referred to as the line of response (LOR). Summing many such events results in quantities that approximate line integrals through the radio-isotope distribution (Ollinger & Fessler (1997)). For 2D imaging these line integrals form a discrete approximation of the Radon transform (Deans (1983)) of a cross-section of the radio-isotope concentration, and can be inverted to form an image of the radioisotope distribution. A schematic diagram of a PET tomograph is shown in Figure 2.1.

2.1 Detectors

The most critical components in a PET tomograph are the detectors (Dahlbom & Hoffman (1988)). Detectors are arranged in blocks as shown in Figure 2.2. Detector blocks are formed by optically coupling a rectangular bundle of crystals to one or more photomultiplier tubes (PMTs). When a photon is incident on the crystal, electrons are moved from the valence band to the conduction band. Light is emitted as these electrons return to

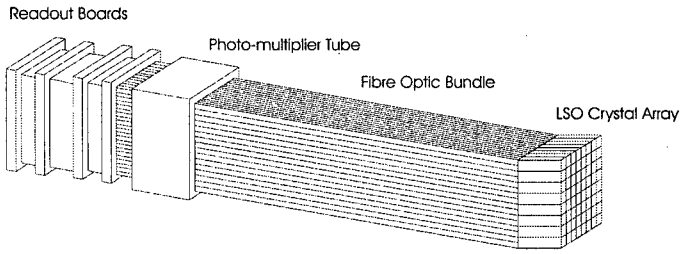

Figure 2.2: A schematic of a detector from the microPET R4 system. Consisting of an 8 x 8 LSO array, 10 cm fibre optic bundle, and a Hamamatsu R5900-C8 position sensitive photo-multiplier tube (PS-PMT). With the readout boards attached to the rear of the tube.

the valence band at impurities in the crystal. Since impurities in the crystal usually have meta-stable excited states, the light output decays exponentially at a rate characteristic to the crystal. The ideal crystal has: (1) high density, so that a large fraction of incident photons scintillate, (2) high light output, for positioning accuracy, (3) fast rise time, for accurate timing, and (4) a short decay time, so that high counting rates can be handled (Ollinger & Fessler (1997)). The block is fabricated in such a way that the amount of light collected by each PMT varies uniquely depending on the crystal in which the scintillation occurred (Dahlbom & Hoffman (1988)). Hence, integrals of the PMT outputs can be decoded to yield the position of each scintillation. The sum of the integrated PMT outputs is proportional to the energy deposited in the crystal. The microPET R4 scanner used in this study uses blocks of lutetium oxyorthosilicate (LSO) crystals, arranged in an 8 x 8 array, fibre-optically coupled to a single position sensitive photomultiplier tube (PS-PMT). Each crystal is 2.1 mm wide in the transverse plane, 2.1 mm wide in the axial dimension and 10 mm deep.

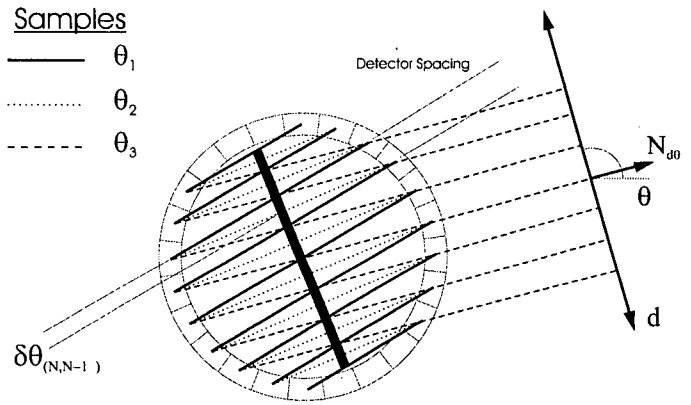

Figure 2.3: Sampling pattern in the transaxial plane for a PET tomograph. Each segment in the detector ring represents one crystal. The solid lines show the parallel projections for the first angle, the dotted lines for the second angle, and the dashed lines for the third angle.

2.2 Resolution

When data is acquired in the 2D slice-collimated mode, the LORs connecting crystals can be binned into sets of parallel projections at evenly spaced angles, as shown in Figure 2.3. Two characteristics are evident. First, samples are unevenly spaced, with finer sampling at the edges of the field of view than at the center. Second, the samples along the heavy line at angles one (θ_1) and three (θ_3) are offset from the samples at angle two (θ_2) by one-half of the detector spacing ($\delta\theta_{N,N-1}$). Therefore, adjacent parallel projections can be combined to yield one-half the number of projection angles with a sampling distance of one-half the detector width (Ollinger & Fessler (1997)).

The Nyquist criterion states that the sampling distance be one-half the spatial resolution, expressed as the full-width-at-half-maximum (FWHM). The full-width-at-half-maximum is defined as the distance between the half-value points of the impulse response. This is the minimum separation required to resolve two distinct points. Hence, the microPET R4

detector block would support a spatial resolution of 2.1 mm. In fact, a tomograph with this crystal size has a measured resolution that is somewhat worse; varying from 1.8 mm at the center of the field of view, to 2.5 mm at the edge.

The best obtainable resolution is termed the intrinsic resolution. This resolution is rarely achieved in practice because unfiltered images are usually very noisy. Typical tomographs have intrinsic resolution of less than 5 mm, the final resolution of the image usually being greater than 8 mm. This is because the reconstruction algorithms trade off resolution for reduced image variance. This final resolution is called the reconstructed resolution. Therefore, the resolution of PET images as they are typically used is not determined by the detectors, but by the degree to which resolution must be degraded to achieve an acceptable image variance. Since the variance is determined by the number of counts that can be collected during the scan, the constraints that govern the resolution of PET images are the amount of radioactivity used, the scan duration, the sensitivity of the tomograph, and the count-rate capability of the tomograph (Ollinger & Fessler (1997)).

2.3 Attenuation

For an incident 511 keV photon there are two possible interactions; photoelectric absorption, and Compton scatter. In materials with low atomic numbers the incidence of photoelectric absorption, for 511 keV photons, is negligible. In a Compton interaction the photon interacts with an outer shell electron. In doing so its path is deflected, and it loses some of its energy. Most scattered photons are scattered out of the field of view and are never detected. The effect of these interactions is termed attenuation. The probability of a photon not interacting as it propagates along the line ℓ, at transverse distance d, and

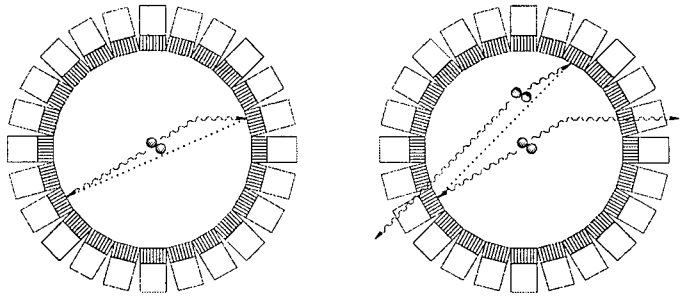

Figure 2.4: Diagram of a scattered event (left) and an accidental coincidence (right). Photons shown leaving the ring are scattered through an oblique angle such that their paths do not intersect a detector.

angle θ is termed the survival probability; and is given by

$$P_{d\theta} = -\int_{\ell} \mu(x)dx \tag{2.1}$$

where μ is the linear attenuation coefficient at position x. The significance of equation (2.1) is that the attenuation experienced by a given pair of annihilation photons is independent of the position of their annihilation along the LOR. This makes possible a simple pre-correction of the data (Ollinger & Fessler (1997)).

2.4 Scattered Events

Annihilations in which one or both photons are scattered, but both are still detected, are termed scattered events. This is depicted on the left in Figure 2.4. These events are incorrectly positioned because the photons' paths are no longer collinear. The overall effect is to add an error signal to the data at low spatial frequencies.

Since photons lose some of their energy when they undergo Compton interaction, they can be be discriminated from un-scattered photons by measuring the energy they deposit

in the crystal. Although this measurement is only accurate to within +/- 10% on most tomographs, it can be used with a simple threshold to reject a significant fraction of scattered events (Ollinger & Fessler (1997)).

2.5 Accidental Coincidences

With so many scattered photons and the relatively small solid angle presented by the detector ring, it is apparent that for many annihilations only one of the photons will be detected. These events are termed singles. If two singles arising from separate annihilations are detected within the same coincidence timing window, they will be recorded as shown on the right side of Figure 2.4. These events are termed accidental coincidences, or randoms. The rate of accidental coincidences can be related to the singles rate by noting that for each single detected at detector i, on average τR_j singles occur at detector j during the coincidence timing window τ; where R_j is the singles rate at detector j. Since each of these τR_j singles results in a coincidence, there are $\tau R_i R_j$ coincidences per unit time for which the first detected photon is incident on detector i. The total number of accidental coincidences is the sum of those for which the first photon is detected at detector j and those for which the first photon is detected at detector i. Hence, the rate of random coincidences along the LOR connecting detectors i and j is given by

$$R_r = 2\tau R_i R_j \tag{2.2}$$

Examination of equation (2.2) shows that reducing the coincidence timing window reduces the counting rate of accidental coincidences. However, timing inaccuracies due to variations in the rise-time of the crystal light output require a timing window of 6-8 ns for LSO. Since the incident singles rates are proportional to the amount of radioactivity, the accidental

coincidence rate increases as the square of the amount of radioactivity in the field of view (for counting rates that do not saturate the detectors). This count-rate limitation, along with detector deadtime, determines the upper limit on the radioactivity used for many studies.

2.6 Detector Deadtime

The time required to process a single event limits the counting rate of a PET scanner (Hoffman et al (1989)). Event processing begins with the rising edge of the pulse for the first detector involved. The pulse is integrated for some time interval, then position calculations and energy discrimination are performed. The detector is "dead" to new events during this time. At very low counting rates, randoms are negligible and the number of true events is linearly related to the amount of activity in the field of view. The number of randoms increase as the square of the radioactivity in the field of view until deadtime becomes significant. Then the number of true events begins to saturate. As the counting rate increases further, the numbers of trues and randoms peak and then decline because of detector saturation. Deadtime is the dominant effect that limits the amount radioactivity used.

2.7 Physical Model

If statistical effects are ignored, these factors can be incorporated into a model for the total number of recorded events to yield

$$Y_{d\theta} = \gamma_{d\theta}[\eta^t_{d\theta} P_{d\theta} M_{d\theta} + \eta^r_{d\theta} r_{d\theta} + \eta^s_{d\theta} s_{d\theta}] \tag{2.3}$$

where $M_{d\theta}$ is the number of annihilations with photons emitted along a LOR (specified by (d, θ) in Figure 2.3), $P_{d\theta}$ is the survival probability, $r_{d\theta}$ is the number of accidental coincidences, $s_{d\theta}$ is the number of scattered events, $\eta^t_{d\theta}$ is the probability of detection for true events, $\eta^r_{d\theta}$ is the probability of detection for accidental coincidences, $\eta^s_{d\theta}$ is the probability of detection for scattered events, and $\gamma_d\theta$ is the probability of an event not being lost due to deadtime. Prior to the emission scan, a transmission scan is performed to characterize the effects of attenuation from the subject. Here a point source containing ^{57}Co rotates around the subject to provide a flux of photons along each line of response. The measured data yield the number of transmitted events, $T_{d\theta}$, along each LOR. Every morning a blank scan , i.e. a transmission scan with nothing in the tomograph, is performed to yield a data set, $B_{d\theta}$. The survival probability is approximated by their ratio: $\hat{P} = \frac{T_{d\theta}}{B_{d\theta}}$. This estimate of survival probabilities would be exact if the data were noiseless. However, they are not noiseless, so they contribute significantly to the overall image variance unless noise reduction algorithms are applied. These algorithms utilize smoothing (Palmer et al (1986)), segmentation and re-projection (Meikle et al (1993), Xu et al (1994)), or statistical image reconstruction and re-projection (Bouman & Sauer (1996), Fessler (1995), Fessler et al (1996), Ollinger (1992)).

A simple way to estimate the accidental coincidences is to note that the arrival times of the photons due to randoms are uniformly distributed in time while those of true coincidences fall within the timing window. Collecting data in a second coincidence timing window that is offset in time, such that it collects no true coincidences, yields data with nearly the same mean as that of the accidental coincidences falling in the trues timing window. The measured data are given by the product $\gamma_{d\theta}\eta^r_{d\theta}r_{d\theta}$, so the detector efficiencies for accidental coincidences, $\eta^r_{d\theta}$, do not have to estimated. Therefore, not only is the method

simple to implement, but it can be performed in hardware before the data are stored. The major drawback of this approach is that the variance of the estimate is of the same order of magnitude as the variance of the data, if a significant fraction of detected events are accidental coincidences. In this case, the subtraction can lead to a significant increase in the variance of the data unless noise reduction methods are used (Casey & Hoffman (1986)). This variance increase can be avoided by counting the number of singles at each detector and using the rate of random coincidences, R_r. Since there are many more singles than true coincidences, the effect on variance is relatively minor. This approach is not widely used because of the additional requirements placed on the acquisition hardware, and because singles rates often vary over the course of an acquisition.

The detector efficiencies for true and scattered events are estimated from a scan of a calibration source with known characteristics (Hoffman et al (1989)). Deadtime is dependent on many factors related to the architecture and design of a specific machine, so its estimation is tailored to the tomograph (Daube-Witherspoon & Carson (1991)). It is usually assumed to be constant over the duration of the scan.

These parameters can be used to estimate the number of emitted photons by using the expression

$$\hat{M}_{d\theta} = \frac{(Y_{d\theta} - R_{d\theta}) - S_{d\theta}}{\gamma_{d\theta}\eta^t_{d\theta}\hat{P}_{d\theta}} \tag{2.4}$$

where we assume that $R_{d\theta} = \gamma_{d\theta}\eta^r_{d\theta}E[r_{d\theta}]$, $S_{d\theta} = \gamma_{d\theta}\eta^s_{d\theta}E[s_{d\theta}]$, and $E[\cdot]$ denotes expectation. The data modeled in equation (2.4) are often stored in 2D arrays with the columns indexed by d and the rows by θ. These data arrays are often called sinograms. This is because, for a point source, d varies sinusoidally with θ.

2.8 Filtered Backprojection

One way to simplify the problem is to ignore the measurement noise altogether, and to assume that the measured data approximate line integrals through the radioisotope distribution. This leads to the classical filtered-backprojection (FBP) method for tomographic image reconstruction (Kak & Slaney (1988)). This method is routinely used for x-ray CT, as well as for PET and SPECT (Single Photon Emission Computed Tomography). Its popularity stems from its computational simplicity, and not because of any advantage in image quality. A mathematical description of filtered backprojection is provided in Appendix A.

Chapter 3

Materials and Methods

The portable closed-loop system used for these experiments consists of a 120 L tank, a centrifugal pump, a bypass loop, two magnetic flow meters, two pressure transducers, a test section and valves for control. The test section is made of clear polycarbonate pipe 70 mm in diameter and 1.1 m in length. The inlet pipe is 14 mm in diameter, forming a 1:5 axisymmetric sudden expansion. Figure 3.1 shows a cross-sectional view of the abrupt expansion.

Flow reaches and leaves the test section through 4.5 m of reinforced hose, which ensures

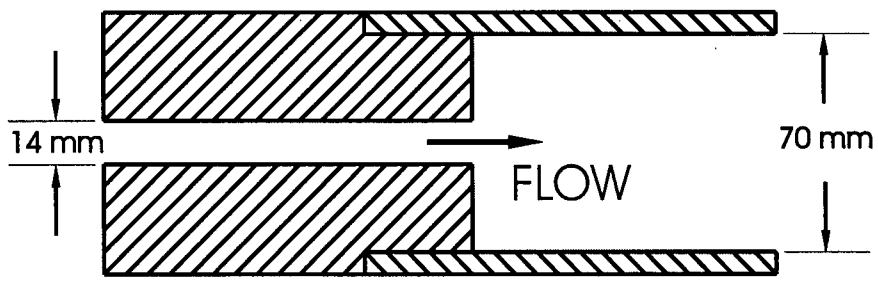

Figure 3.1: A schematic of the sudden expansion.

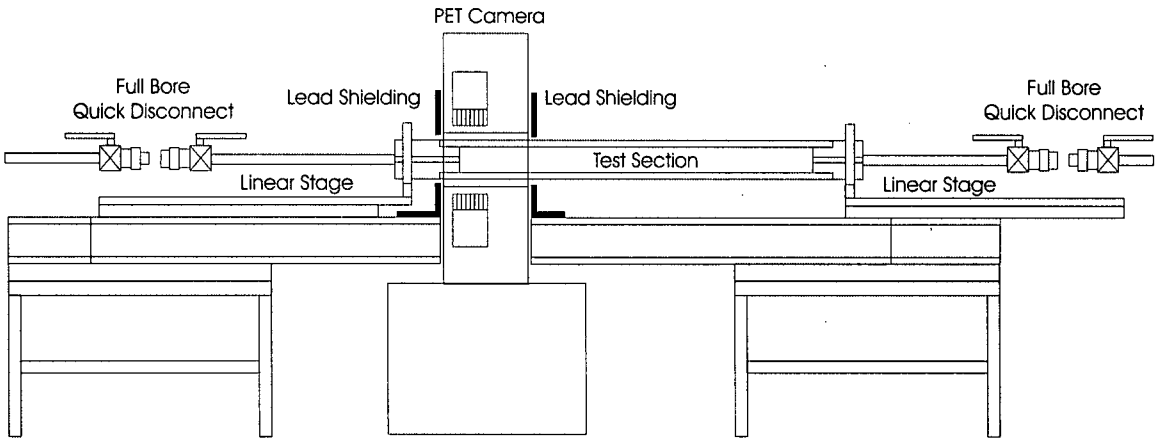

Figure 3.2: A schematic of the experimental setup.

fully developed flow at the expansion step for all cases studied. Both ends of the test section are terminated with a pair of full-bore ball valves and a full-bore quick-disconnect coupling to facilitate placement and removal of the test section into the gantry of the tomograph. The test section is mounted to 760 mm linear stages on either side of the tomograph so that the test section can be moved along its axis. To shield the detector blocks from radiation originating outside the tomograph 19 mm thick lead shielding is positioned concentrically with the test section, butted up against the camera. This thickness of lead stops $\sim$ 95% of incoming 511 keV gamma photons. Figure 3.2 is a schematic of the experimental setup and Figure 3.3 represents the portable flow loop.

The experiments were conducted by first radioactively labelling a selected Bauer-McNett fraction of TMP fibres with ^{18}F and introducing them into a non-radioactive pulp suspension. The fibre length of each fraction of fibres and the whole suspension, as determined through use of an optical fibre analyzer, are provided in Figure 3.4. As shown, the names of the fibre fractions are defined using the screen sizes by which they were retained in the Bauer-McNett device. This is the traditional method of defining fibre fractions in the pulp

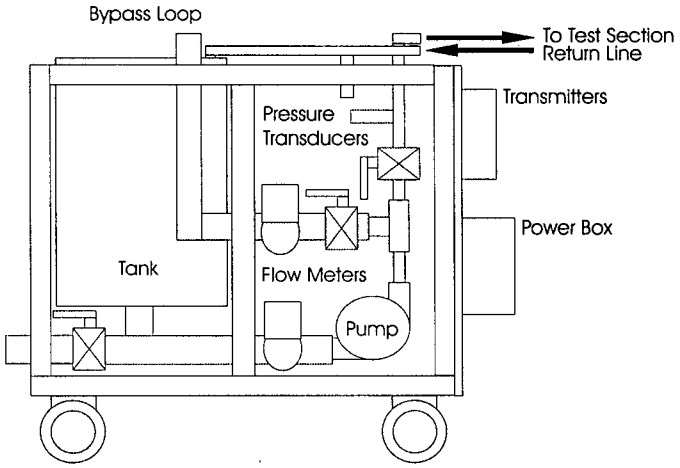

Figure 3.3: A schematic of the portable flow loop.

and paper literature. The fibres were labeled by suspending them in a solution of acetic acid while $^{18}F - F_2$ was bubbled through the suspension at 10 ml/min with constant stirring. After the addition of the fluorine the fibres were filtered and washed with distilled water. At this point the fibres were labeled with ^{18}F with a 10% yield based upon the total radioactivity introduced. ^{18}F has been chosen here in preference to other positron emitting tracers such as ^{15}O, ^{11}C, or ^{13}N because of its reasonably long half-life of 110 minutes and its reactivity with TMP pulp fibres.

The tomograph used in this study is the Concorde Microsystems microPET R4. The microPET Rodent 4-ring system (R4) has a 7.8 *cm* axial extent, a 10 *cm* transaxial field of view (FOV) and a 12 *cm* gantry aperture. The system is composed of 96 detector modules, each with an 8 x 8 array of 2.1 x 2.1 x 10 *mm* lutetium oxyorthosilicate (LSO) crystals, arranged in 32 crystal rings 14.8 *cm* in diameter. Each of the detector crystals are coupled to a Hamamatsu R5900-C8 position sensitive photomultiplier tube (PS-PMT) via a 10 *cm* long optical fibre bundle. The detectors have a timing resolution of 3.2 *ns*, an average

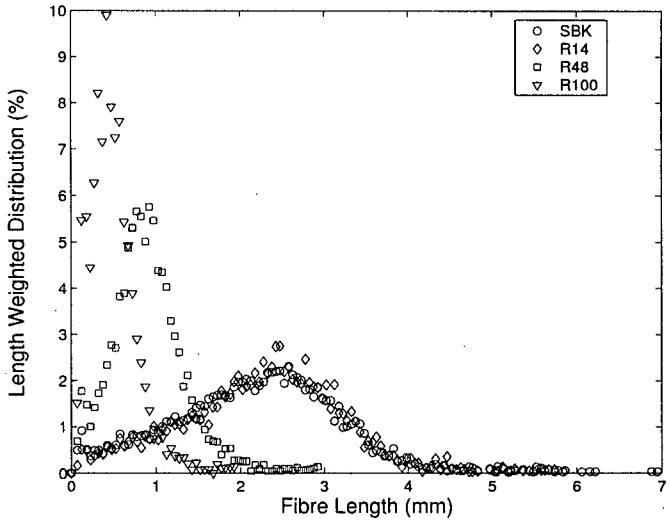

Figure 3.4: The fibre length distributions of the SBK pulp and the three tracer fibres used (labeled R14,R48 and R100). The nomenclature for the fibre fractions is retained from the Bauer Mcnett device used to separate the fibre suspension.

energy resolution of 18.45%, and an average intrinsic spatial resolution of 1.75 *mm*. The system operates in 3D mode without inter-plane septa, acquiring data in list mode. Using the 2D filtered back projection reconstruction algorithm, the resolution in the centre of the field of view (FOV) is 2.03 *mm* FWHM in the tangential direction (horizontal direction of the FOV), and 2.07 *mm* FWHM in the radial direction (vertical direction of the FOV). The tangential resolution slowly increases to 3.38 *mm* FWHM at the edge of the FOV. The radial resolution increases to 3.00 *mm* FWHM at 25 *mm* radial offset and then deteriorates linearly to 3.68 *mm* FWHM at the edge of the FOV (Mok et al (2003)). All images in this study were reconstructed using the 2D filtered back projection algorithm.

Before beginning a series of scans with pulp we started with three test scans using water and ^{11}C[methyl-iodide]. The purpose of the preliminary scans were two fold. Firstly, we wanted to characterize the effect of having $\sim$ 95% of the activity located outside of the tomograph's

field of view; and secondly, to find out the count-rate capability of the tomograph with our particular apparatus. In the first scan we set up the flow loop and filled the tank with 40 L of water and added 3880 MBq of ^{11}C[methyl-iodide]. The acquisition was run for 2.5 hours (7 half-lives). After reconstructing the data we found that the activity had decayed much faster than expected. We discovered that the boiling point of ^{11}C[methyl-iodide] was ~26 °C and that the activity was volatile. In our second scan we set up a sealed sudden pipe expansion with the same diametrical dimensions as the test section, but shortened to 30 *cm* in length. The new phantom was filled with water and 330 MBq of ^{11}C[methyl-iodide] and scanned for 2.5 hours. The results indicated that the tomograph had trouble with very high and very low count rates. After 3.3 half-lives the the tomograph was able to measure the activity in the phantom, and thereafter for a period of 3.3 half-lives. For 40 L of pulp suspension this translates into a maximum activity of 1110 MBq and a minimum of 110 MBq. With this data we repeated the first scan with 1000 MBq of ^{11}C[methyl-iodide] in solution with a sodium bicarbonate buffer to prevent the activity from becoming volatile. The results were good and the activity levels confirmed for the subsequent series of pulp scans.

Table 3.1 provides the fraction labeled, the upstream bulk flow rate, duration of scans, and activity added for each image successfully obtained in this study. For each case an image was captured at the step and another 70 *cm* downstream of the expansion. Each scan begins with the production of the labeled fraction. Meanwhile, the flow-loop is set up around the tomograph. After the test section has been placed in the gantry aperture of the tomograph and plumbed in, it is positioned in the tomograph's field of view with the aid of a laser line. Prior to the emission scan a transmission scan is performed to characterize the effects of attenuation of the photons, due to the test section and its contents. Here

Scan	Tracer (fraction)	Upstream Vel. (m/s)	Activity (MBq)	Image Dur. Step (s)	Image Dur. Downstream (s)	Phenom. Behaviour
1	R48	0.5	585	3599	2736	plug
2	R48	0.7	480	2212	2922	fluidized
3	R48	0.8	1125	2708	2289	fluidized
4	R14	0.5	1015	2573	2197	partially-fluidized
5	R14	0.9	1045	1220	1134	fluidized
6	R100	0.9	475	2772	3072	fluidized

Table 3.1: A summary of the scans conducted.

a rotating point source containing ^{57}Co rotates around the object to provide a flux of photons along each line of response. Before the activity is introduced, the pump is turned on and the system allowed to run for several minutes. Before the labeled fibres are added to the tank the flow rate is adjusted and the camera set to acquire data. The radioactive fibres are then added to the tank and allowed to be pumped though the system. At this point data acquisition has begun. Each scan is allowed to run until 100,000,000 events are detected or one hour has elapsed.

Chapter 4

Results and Discussion

The concentration profiles were obtained at various upstream velocities for suspensions with a bulk concentration of 0.4 %(wt) with three different tracer fibre sizes. As the number of trials conducted was small, most figures have been included. The discussion of the results will be conducted in three subsections. In the first subsection we will discuss the impact of velocity on the concentration distribution. In the second subsection we examine the effect of tracer particle size on the measured profile. Finally, we report the results far downstream of the expansion.

4.1 The Effect of Velocity

In this section we discuss the qualitative behavior of this suspension as a function of velocity. As shown in Table 3.1, we recorded four cases in which the tracer fibres were well mixed after the expansion. We defined these cases as "fluidized", and the observed

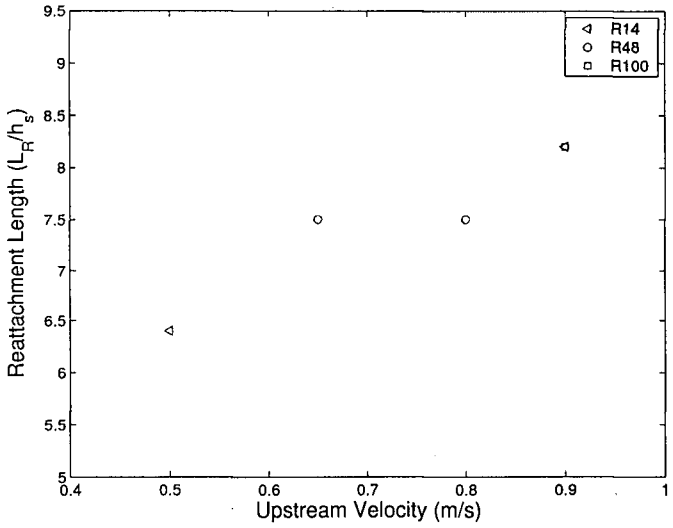

Figure 4.1: Estimates of the size of the recirculation zone for the cases in which the suspension was fluidized after the expansion. h_s is the step height.

flow was qualitatively similar to that reported by Salmela & Kataja (2005). The size of the recirculation zone is shown in Figure 4.1 for these cases only. It should be noted that the length of the recirculation zone L_R has been scaled to the height of the step h_s. It is difficult to compare our results quantitatively to either those reported by Salmela & Kataja (2005), as we have a different step size and suspension concentration, or to those for a corresponding Bingham fluid, as the rheological properties of the suspension are difficult to characterize properly.

We begin the discussion of the effect of velocity by examining Scan 2, see Table 3.1 and Figure 4.2. As with all cases presented three views are provided; a top view, a side view, and a cross-sectional view. The top and side views are slices from the centre of the test section in planes orthogonal to the viewing direction. As shown, these images are qualitatively similar to those reported by Moraczewski et al (2005) in that we see a central jet surrounded by a recirculating zone. There are three observations that can be

made immediately from this result. First, the fibres are not distributed evenly through the imaged-volume. An asymmetry is apparent in Figure 4.2(c) in which there is a higher concentration of tracer fibres at the bottom of the tube when compared to the top. This feature was found in all fluidized cases examined. As the images were integrated over some time the temporal evolution of this concentration asymmetry is not known. Rebinning the datasets into shorter duration frames may provide insight into this particle accumulation. However, with a reduced number of events in each frame much higher levels of noise are to be expected. Second, there is an annular region between the jet and the recirculation zone with a concentration that is lower than the average concentration of the suspension. In other words, we observe a region with particle depletion. Finally, in the centre of the recirculation zones the concentration of tracer fibres is significantly larger than the average concentration. The last two observations have been reported by Moraczewski et al (2005). We attempt to quantify these features by examining the radial concentration profiles at different axial positions, see Figure 4.3 (a) and (b). In these figures we have normalized the concentration to the bulk concentration of the suspension, i.e. 0.4 wt%. Radial and axial distances have been normalized by the radius of the larger pipe; and the axial origin, $x = 0$, is set at the step. The horizontal and vertical axes are y and z, respectively, and their origin is placed along the central axis of the test section. We speculate that the concentration-depletion zone results from the water layer formed in the upstream tube. It is commonly understood that a water layer forms on the periphery of a pipe with a flowing pulp fibre suspension. We have characterized both the radius of the jet and thickness of the concentration-depletion layer in Figure 4.3(c) as a function of axial position. As shown, we see that the radius of the jet remains essentially constant over the distance reported, while the size of the concentration-depletion layer decreases slightly. Finally, as shown in Figure

4.3(d) the average concentration of the jet increases with axial position. In this case we see a 50% increase in the concentration in the central portion of the tube and advance the argument that this results from the deceleration of the jet.

At this point we turn our attention to the second type of behavior observed, i.e. plug flow. We observed this in one of the scans conducted; namely Scan 1, which was conducted at an upstream velocity of 0.5 m/s. As shown in Figure 4.4, the tracer fibres were not well distributed after the expansion plane and traveled through the region visualized as a plug. Clearly at this lower velocity the shear imparted by the fluid is insufficient to disrupt the fibre network. It must be noted that during imaging, the central jet may be slowly meandering or folding as it travels down the length of the tube. This feature can not be captured as the image acquired is averaged over some time. We characterize these curves by showing the radial concentrations and the size of the central jet in Figure 4.5. As shown, we see that the tracer fibres spread radially with increasing axial distance. The mechanism by which these fibres spread is difficult, if not impossible, to ascertain from these figures alone as the jet may meander during the imaging period. In other words, we can not ascertain if the tracer fibre mixing results from shear induced migration or from the stability of the jet. One of the striking features in this image is the relatively large localized concentration of activity near the top of the tube in Figure 4.5(c). We are uncertain of the origin of this but its presence confirms the fact that mixing does not take place at this velocity. The tracer fibres that accumulated at the top of the tube may have done so gradually, or may have arrived as a floc. Rebinning the dataset into frames of shorter duration would allow the evolution of the accumulation to be examined. This, however, would result in images and data with higher noise content due to the reduced number of events in each rebinned frame.

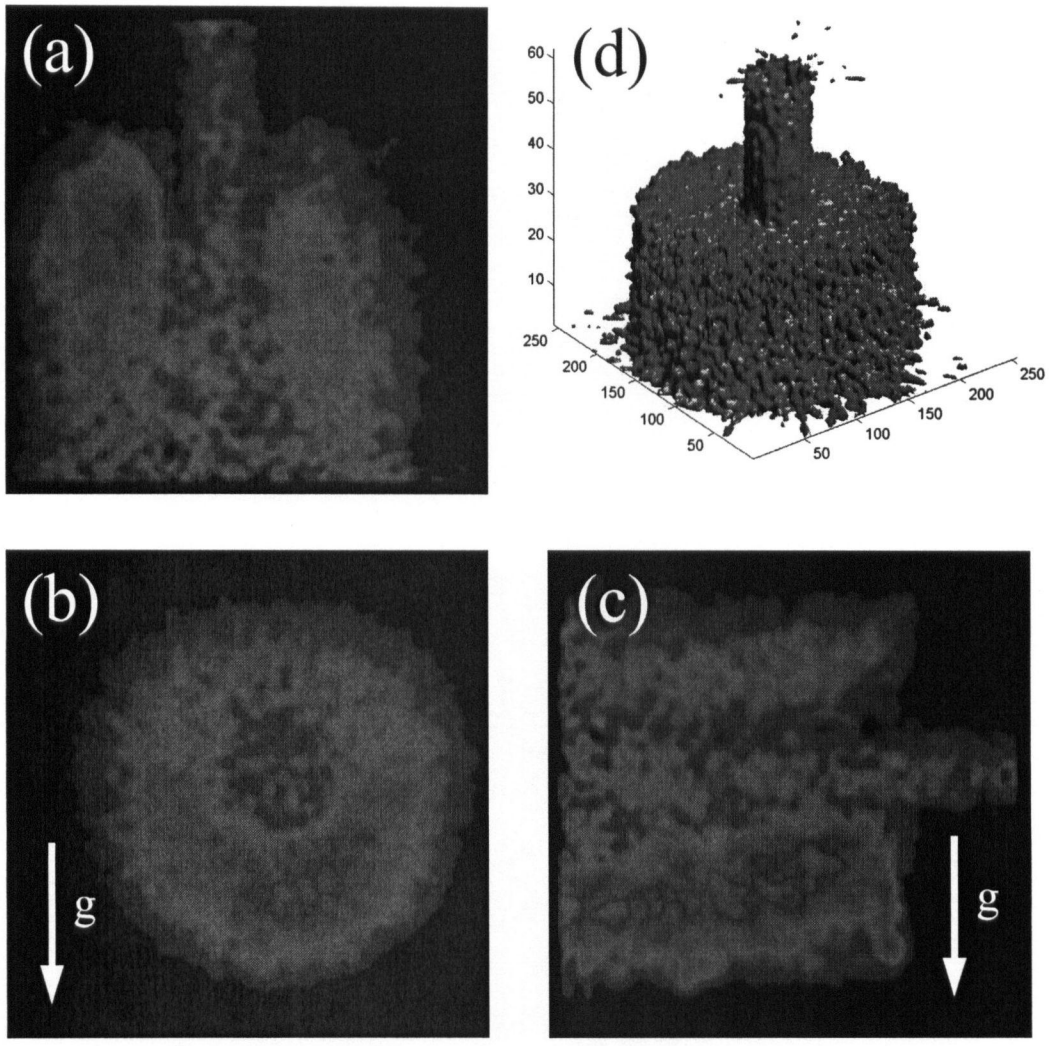

Figure 4.2: Four views of the activity profile for the case in which the tracer fibres were well-mixed, or fluidized, after the expansion. The image was acquired using the R48 tracer fibres with the upstream velocity set at 0.7 m/s (see Table 3.1). Image (a) represents the top view, (b) is a cross-sectional view at $x/R_o = 0.57$, (c) is a side view, and (d) is a three-dimensional reconstruction of the activity distribution.

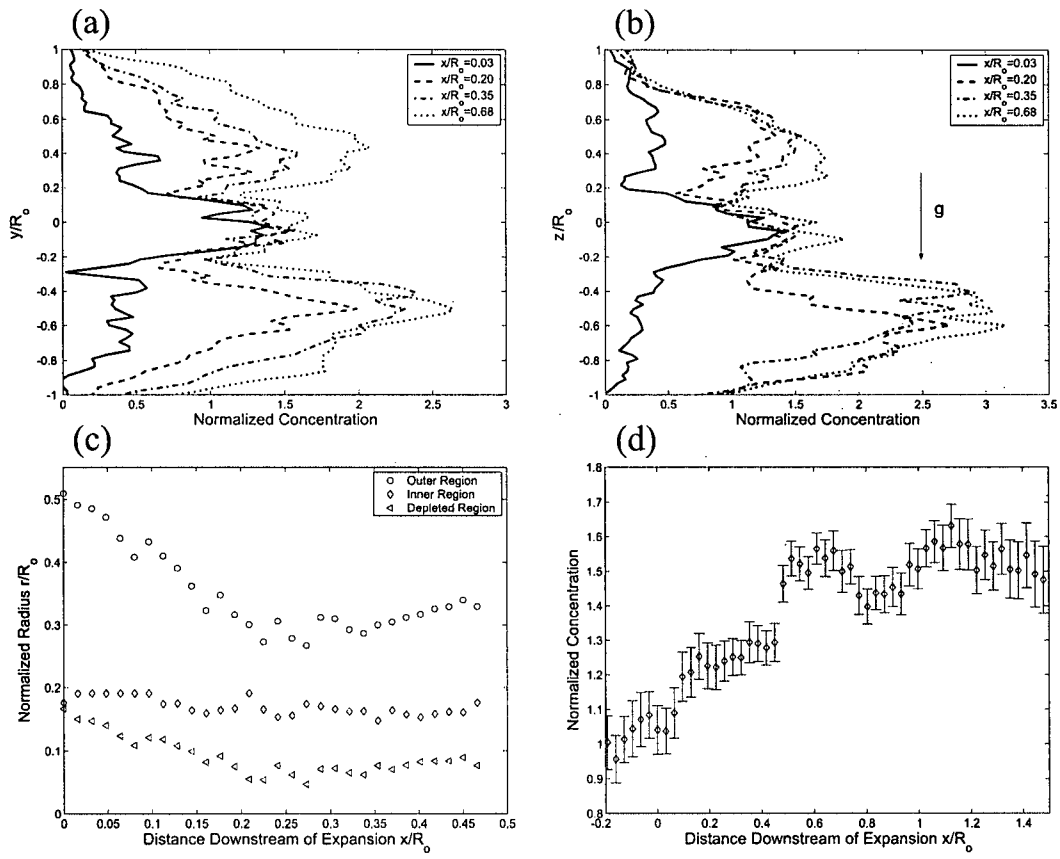

Figure 4.3: Four views of the activity profile for the case in which the tracer fibres were well-mixed, or fluidized, after the expansion. The image was acquired using the R48 tracer fibres with the upstream velocity set at 0.7 m/s (see Table 3.1). Image (a) represents the concentration profile in the radial direction for a central horizontal slice at four different axial positions. Image (b) represents the concentration profile in the radial direction from a central vertical slice at four different axial positions. Image (c) is an estimate of the growth of the depletion zone. Estimates are given of the inner and outer radii of the depletion zone and their difference. Image (d) is an estimate of the average concentration of the jet as a function of axial position.

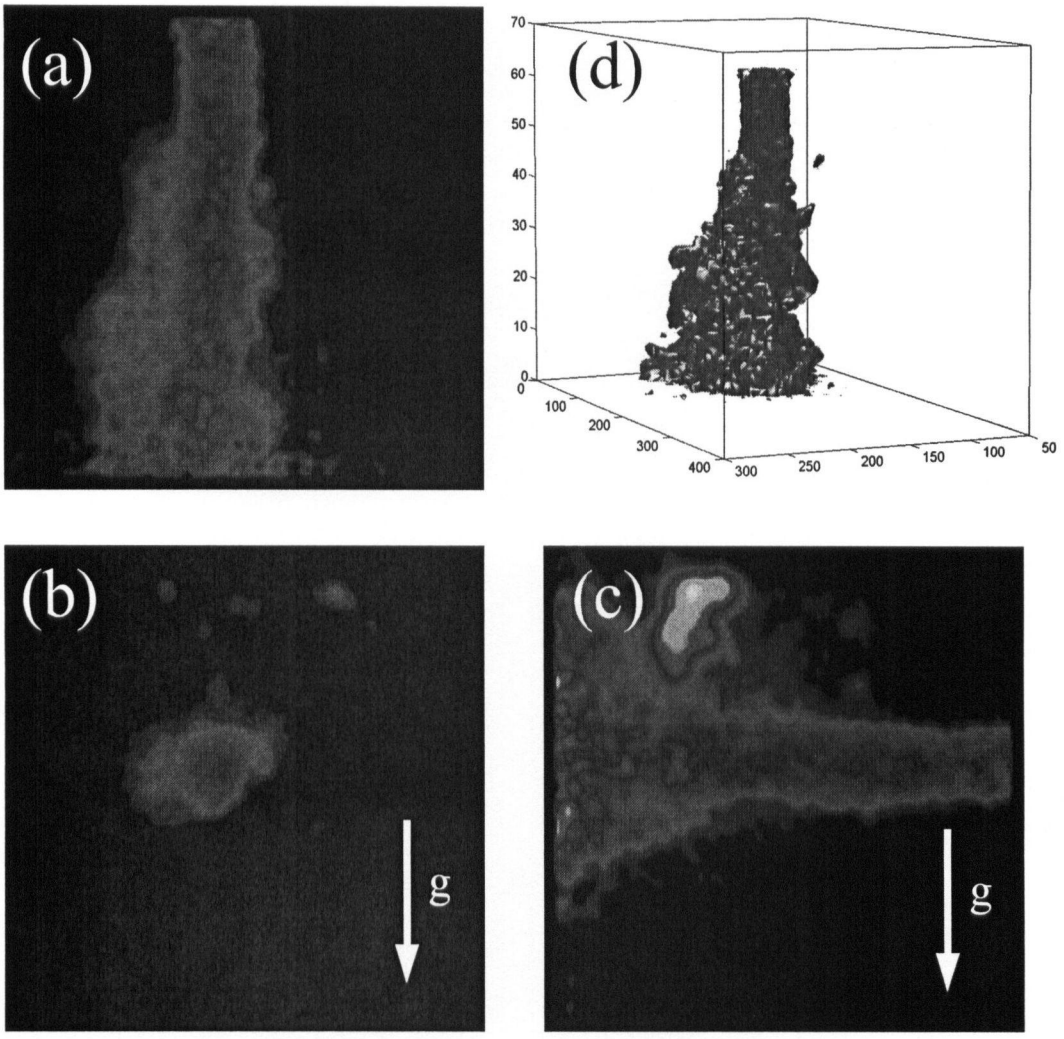

Figure 4.4: Four views of the activity profile for the case in which the tracer fibres were not well-mixed after the expansion. We define this case as plug flow type behavior. The image was acquired using the R48 tracer fibres with the upstream velocity set at 0.5 m/s (see Table 3.1). Image (a) represents the top view, (b) is a cross-sectional view at $x/R_o = 1.00$, (c) is a side view, and (d) is a three-dimensional reconstruction of the activity distribution.

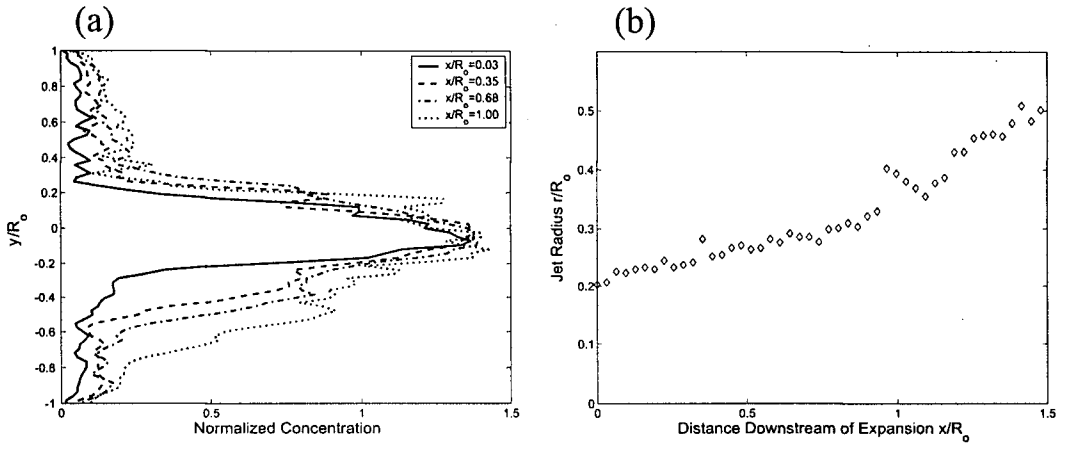

Figure 4.5: A view of the activity profile and jet expansion for the case in which the tracer fibres were not well-mixed after the expansion. The figures are from the image acquired using the R48 tracer fibres with the upstream velocity set at 0.5 m/s (see Table 3.1). Image (a) represents the concentration profile in the radial direction from a central horizontal slice at four different axial positions. Image (b) represents the width of the activity profile as a function of axial position.

4.2 Effect of Particle Size

At this point we compare the effect of particle size by examining two cases conducted at the same velocities using different length fractions. In the first comparison, we examine scans 5 and 6 in which we compare the distribution of the R100 and R14 tracer fibres at 0.9 m/s (see Figure 4.6). As shown, the activity distribution of these tracer fibres appear somewhat similar. In both cases the features reported in the previous section are apparent; that is an asymmetry in the vertical direction, a depletion layer between the central jet and the recirculation zone, and particle accumulation in the lower recirculating zone. We find that no significant differences in the distributions are apparent between these two cases.

In the second comparison, we examine the distributions of the R48 and R14 fibres at 0.5 m/s as given as scans 1 and 4 in Table 3.1. The results for scan 1 have been shown

earlier as Figure 4.4. Here it is apparent that the tracer fibres are not well-mixed after the expansion. With the R14 fibres however, we find that the tracer fibres are well-mixed in the upper portion of the channel only (see Figure 4.7). In the upper portion of the channel we observe the depletion zone between the central jet and the outer portions of the channel. It should be noted that during this trial it was visually observed that the lower portion of the channel was static. We do not interpret these results as quantitative evidence that their is a difference between the motion of these two classes of fibres. We speculate that this result occurred due to the fact that the experimental protocol was not the same as the other scans. The pulp in the test section was allowed to settle over several days prior to the scan and was not well mixed prior to the start of the scan. Furthermore, when the scan was conducted the flow rate began high and was lowered, as opposed to being ramped up to the targeted flow rate as in subsequent scans. This resulted in the region with lower fibre concentration being fluidized first, and when the flow rate was dropped this region remained in motion. We have included this result as it is interesting to report the possibility of a stable, static region in this type of device.

4.3 Far Downstream

Far downstream of the expansion ($x/R_o = 20$) we were able to measure both the concentration distribution using PET and the velocity profile using ultrasound Doppler velocimetry (UDV), a commercial device obtained from Signal Processing SA. For all flowrates tested, the velocity profiles at this point were similar and displayed plug like behaviour. As shown in Figure 4.8, a velocity boundary layer exists near the walls of the pipe in the region $|y/R_o| > 0.8$. We display the concentration profiles at this point for four different cases

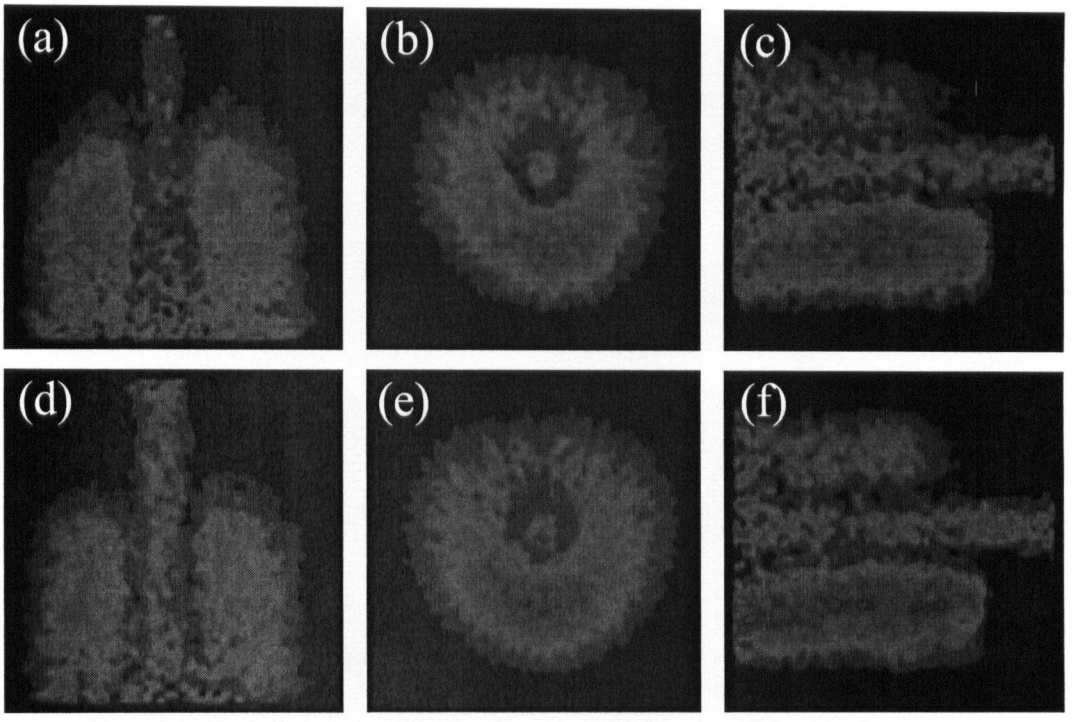

Figure 4.6: Two cases in which the tracer fibres were well-mixed after the expansion. In images (a)-(c) we examine the case in which the upstream velocity was set at 0.9 m/s with the R100 tracer fibres. Images (d)-(f) represent the case with the R14 tracer fibres. The images in the first column ((a) and ((d)) represent the top view. The images in the second column represent the cross-sectional view at $x/R_o = 0.57$. The remaining two images represent the side view.

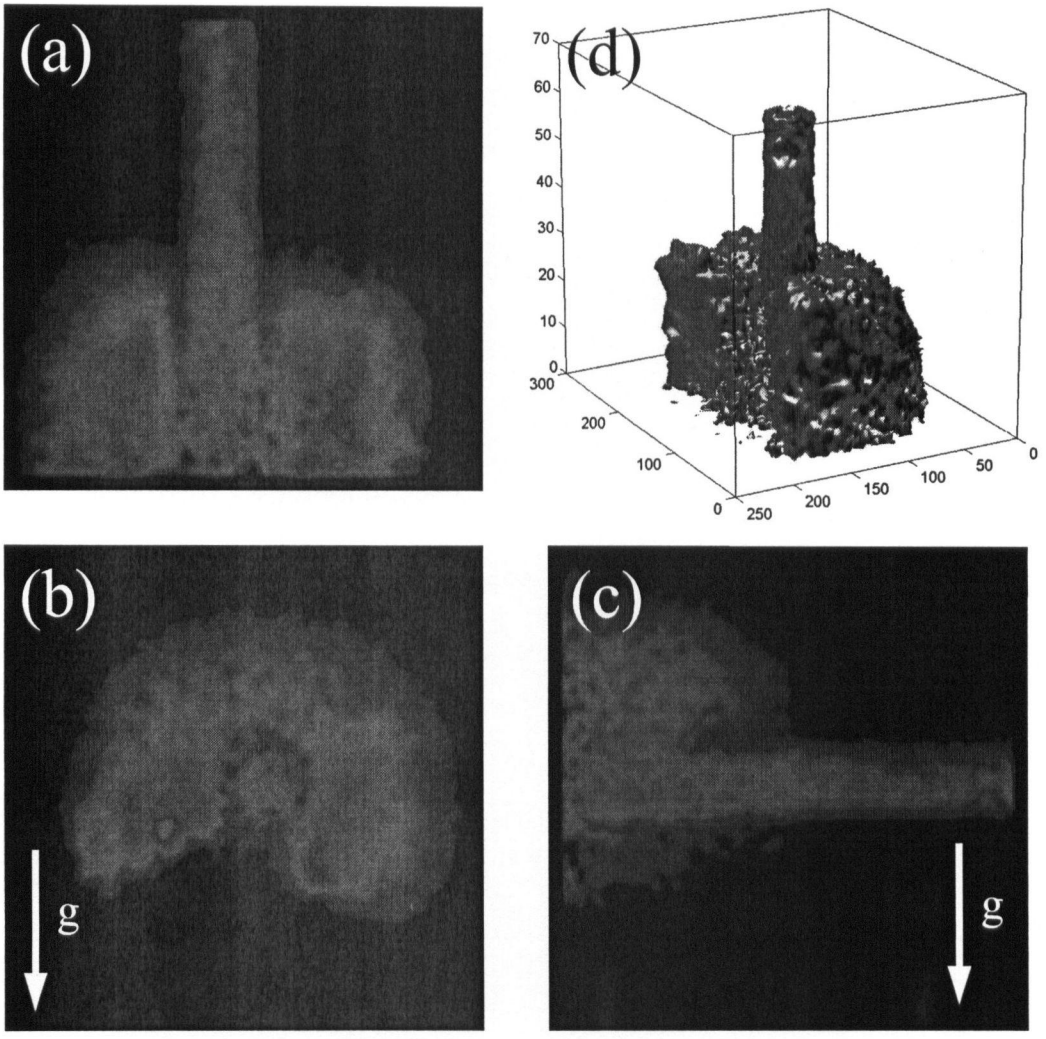

Figure 4.7: Four views of the activity profile for the case in which the tracer fibres were partially-mixed after the expansion. The image was acquired using the R14 tracer fibres with the upstream velocity set at 0.5 m/s (see Table 3.1). Image (a) represents the top view, (b) is a cross-sectional view at $x/R_o = 0.57$, (c) is a side view, and (d) is a three-dimensional reconstruction of the activity distribution.

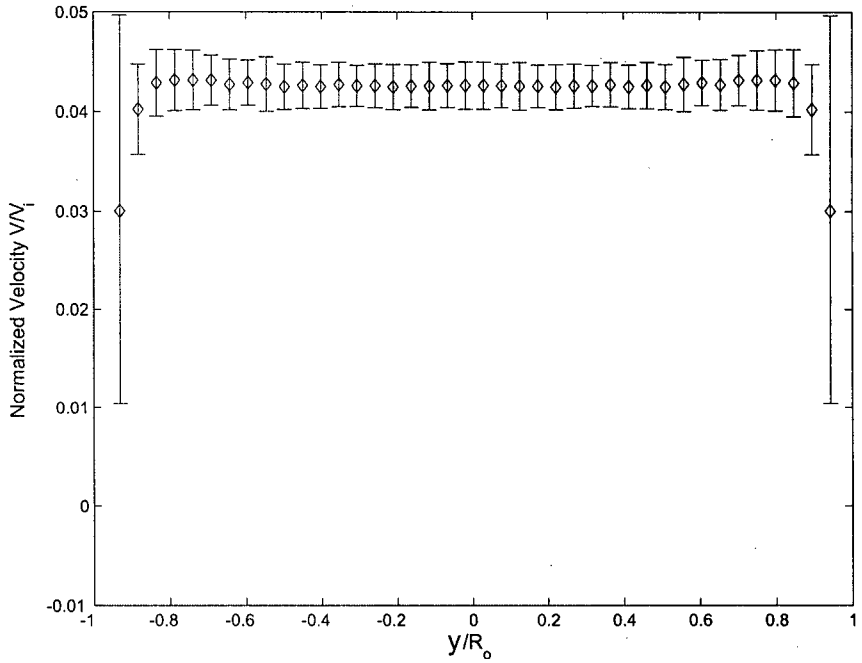

Figure 4.8: The velocity profile of the suspension as measured using UDV. Six experiments were conducted in which the upstream velocity V_i set in the range from 0.5 to 1.0 m/s. The error bars represents the standard deviation determined from the average of this data set.

(see Figure 4.9). What is apparent from these figures is that the concentration profile is not necessarily similar to the velocity profile. We speculate that the tracer fibres, trapped in small flocs at the inlet, are not sufficiently disrupted by the shear at the step to re-distribute themselves evenly downstream. As the flow rate is increased more mixing is induced and a more even radial distribution is evident.

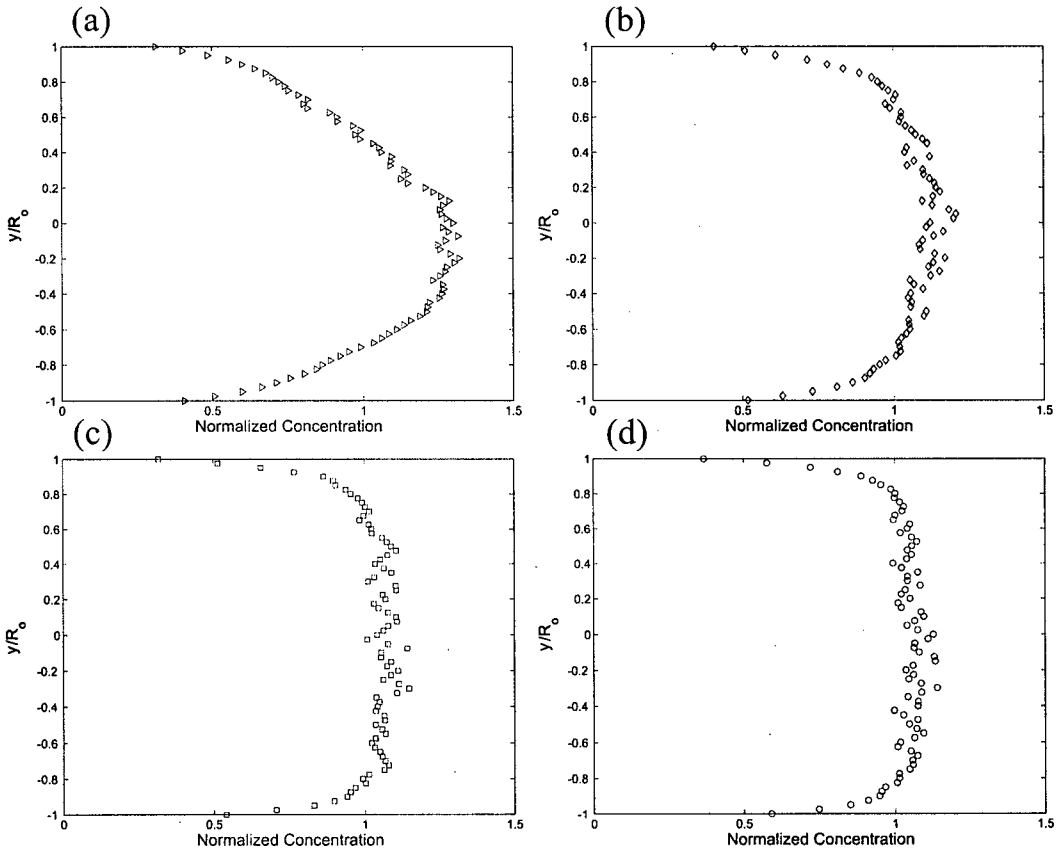

Figure 4.9: The concentration profile downstream of the expansion. (a) Scan 1, (b) Scan 2, (c) Scan 5 and (d) Scan 6. Details of each experiment are given in Table 3.1.

Chapter 5

Summary and Conclusion

Positron Emission Tomography (PET) was used to investigate the dynamics of a 0.4% (wt) fibre suspension flowing through an axisymmetric 1:5 sudden expansion. Six scans were conducted in which both the upstream velocity and the size of tracer fibres labelled were varied. Images were taken upstream and downstream of the expansion plane with the upstream velocity being varied from 0.5 to 0.9 m/s. The expansion plane imparts shear that disrupts the fibre network causing measurable changes in the local fibre concentration. Two distinct regions were clearly distinguished: plug like, in which the tracer fibres were not mixed through the entire volume of the expansion; and fluidized, in which the tracer fibres were well mixed. Our results for the fluidized case are worth highlighting as we found that concentration inhomogeneities exist. These inhomogeneities are exemplified by the fibre depleted annulus surrounding the incoming jet, the densification of the jet immediately downstream of the expansion and the vertical asymmetry in the recirculation region. Rebinning the datasets into shorter duration frames may provide insight into the

evolution of the concentration asymmetries, provided there are sufficient counts in each frame to yield data with acceptable noise levels. We consider these to be the most significant findings in this work but are as yet unable to develop a mechanistic understanding of these phenomena.

Bibliography

ALTOBELLI, S. A. FUKUSHIMA E. & MONDY, L.A. 1997 Nuclear magnetic resonance imaging of particle migration in suspensions undergoing extrusion *J. Rheol.* **41(5)**, 1105-1115

ALTOBELLI, S. A. GIVLER, R. C. & FUKUSHIMA, E. 1997 Velocity and concentration measurements of suspensions by nuclear magnetic resonance imaging *J. Rheol.* **35(5)**, 721-734

AROLA, D. POWELL, R. MCCARTHY, M. LI, T.-Q. & ÖDBERG, L. 1998 NMR Imaging of Pulp Suspension Flowing through an Abrupt Pipe Expansion *AIChE J.* **44(12)**, 2597-2606

BOUMAN, C.A., & SAUER, K., 1996 A Unified Approach to Statistical Tomography Using Coordinate Descent Optimization *IEEE Trans. Imag. Proc.* **5**, 480-492

CASEY, M.E., & HOFFMAN, E.J., 1986 Quantitation in Positron Emission Tomography: 7. A Technique to Reduce Noise in Accidental Coincidence Measurements and Coincidence Efficiency Calibration *J. Computr. Assist. Tomogr.* **10**, 42-50

DAHLBOM, M., & HOFFMAN, E.J., 1988 An Evaluation of a Two-Dimensional Array Detector for High Resolution PET *IEEE Trans. Med. Imag.* **7**, 264-272

DAUBE-WITHERSPOON, M.E., & CARSON, R.E., 1991 Unified Deadtime Correction Model for PET *IEEE Trans. Med. Imag.* **10**, 267-275

DEANS, S.R., 1983 The Radon Transform and Some of its Applications *New York: Wiley*

DEFRISE, M., TOWNSEND, D.W., & CLACK, R., 1989 Three-Dimensional Image Reconstruction from Complete Projections *Phys. Med. Bio.* **34**, 573-587

DUFFY, G.G. & TITCHENER, A.L. 1975 The Disruptive Shear Stress of Pulp Networks *Svensk. Papperstidn.* **13**, 474-479

FESSLER, J.A., 1995 Hybrid Poisson/polynomial Objective Functions for Tomographic Image Reconstruction from Transmission Scans *IEEE Trans. Imag. Proc.* **4**, 1439-1450

FESSLER, J.A, FICARO, E.P., CLINTHORNE, N.H., & LANGE, K., 1996 Grouped-coordinate Ascent Algorithms for Penalized-likelihood Transmission Image Reconstruction *IEEE Trans. Med. Imag.* **16**, 166-175

HAMMAD, K. J., ÖTÜGEN, M. V. VRADIS, G. & ARIK, E 1999 Laminar Flow of a Nonlinear Viscoplastic Fluid Through an Axisymmetric Sudden Expansion *ASME J.* **121**, 488-495

HERMAN, G.T., 1980 Image Reconstruction from Projections *New York Academic Press*

HOFFMAN, E.J., GUERRERO, T.M., GERMANO, G., DIGBY, W.M., & DAHLBOM, M., 1989 PET System Calibration Corrections for Quantitative Spatially Accurate Images *IEEE Trans. Nucl. Sci.* **36**, 1108-1112

JOSSIC, L. BRIGUET, A. & MAGNIN, A. 2002 Segregation under flow of objects suspended in a yield stress fluid and NMR imaging visualization *Chem. Eng. Sci.* **57**, 409-418

KAK, A.C., & SLANEY, M., 1988 Principles of Computerized Tomography *New York*

KARINO, T. & GOLDSMITH, H. L. 1977 Flow behavior of blood-cells and rigid spheres in an annular vortex *Phil.. Trans. R. Soc. London, Ser. B* **279**, 413-445

KEREKES, R. J. SOSZYSNKI, R. M. & TAM DOO, P. M. 1985 The flocculation of pulp fibres *Fund. Res. Symp., Oxford* **1**, 265-310

KINAHAN, P.E., & ROGERS, J.G., 1989 Analytic Three-Dimensional Image Reconstruction Using all Detected Events *IEEE Trans. Nucl. Sci.* **36**, 1108-1112

LATORNELL, D. J., & POLLARD, A. 1986 Some Observations on the Evolution of Shear Layer Instabilities in Laminar Flow Through Axisymmetric Sudden Expansions *Phys. Fluids* **29**, 2828-2835

LEIGHTON, D. & ACRIVOS, A. 1987 The shear-induced migration of particles in concentrated suspensions *J. Fluid Mech.* **181**, 415-439

MACAGNO, E.O. & HUNG, T.K 1967 Computational and Experimental Study of a Captive Annular Eddy *J. Fluid Mech.* **28**, 43-64

MIEKLE, S.R., DAHLBOM, M., $ CHERRY, S.R, 1993 Attenuation Correction Using Count-Limited Transmission Data in Positron Emission Tomography *J. Nucl. Med.* **34**, 143-144

MOK, S-P., WANG, C-H., CHEN, J-C., & LIU, R-S., 2003 Performance Evaluation of the

High Resolution Small Animal PET Scanner *Biomed. Eng. Appl Basis Comm.* **15(4)**, 143-149

MORACZEWSKI, T., TANG, H., & SHAPLEY, N. 2005 Flow of a concentrated suspension through an abrupt axisymmetric expansion measured by nuclear magnetic resonance imaging *J. Rheol.* **49(6)**, 1409-1428

NATTERER, F., 1986 The Mathematics of Computerized Tomography *New York: Wiley*

OLLINGER, J.M., 1992 The Use Of Maximum A Posteriori And Maximum Likelihood Transmission Images For Attenuation Correction In PET *Proc. 1992 IEEE Med. Imag. Conf.* 1185-1187

OLLINGER, J.M., & FESSLER, J.A., 1997 Positron-Emission Tomography *IEEE Signal Pro. Mag.* **14(1)**, 43-55

PALMER, M.R., ROGERS, J.G., BERGSTROM, M., BEDDOES, M.P., & PATE, B.D., 1986 Transmission Profile Filtering for Positron Emission Tomography *IEEE Trans. Nucl. Sci.* **33**, 478-481

PHILLIPS, R. J. ARMSTRONG R. C. BROWN R. A. GRAHAM A. L. & ABBOTT J. R. 1992 A constitutive equation for concentrated suspensions that accounts for shear-induced particle migration *Phys. Fluids* **4**, 30-40

SALMELA, J., & KATAJA, M., 2005 Floc Rupture and Re-Flocculation in Turbulent Shear Flow *Fund. Res. Symp., Cambridge* **1**, 35-50

SHEPP, L.A., & LOGAN, B.F., 1974 The Fourier Reconstruction of a Head Section *IEEE Trans. Nucl. Sci.* **21**, 21-43

THALEN, N. & WAHREN, D. 1964 Shear Modulus and Ultimate Shear Strength of Some Pulp Fibre Networks *Svensk. Papperstidn.* **67(7)**, 259-264

THALEN, N. & WAHREN, D. 1964 An Experimental Investigation of the Shear Modulus of Model Fibre Networks *Svensk. Papperstidn.* **67(11)**, 474-480

XU, M., LUK, W.K., CUTLER, P.D., & DIGBY, W.M., 1994 Local Threshold for Segmented Attenuation Correction of PET Imaging of the Thorax *IEEE Trans. Nucl. Sci.* **41**, 1532-1537

Appendix A

Filtered Backprojection

Filtered backprojection was first applied to PET by Shepp & Logan (1974). Introductory treatments of the algorithm can be found in Kak & Slaney (1988), and Herman (1980). With more comprehensive treatments in Deans (1983), and Natterer (1986). The distribution of the radioisotope is modeled by the function $\lambda(x, y, z) \in L^2$. For a given 2D slice, we assume that the mean of an individual measurement $Y_{d\theta}$ (equation (2.3)) is given by

$$g_\theta(d) = \int_{\ell(d,\theta)} \lambda(x, y, z) dx dy dz \tag{A.1}$$

where $\ell(d, \theta)$ is the line connecting the two detectors involved in the coincidence. In practice, it is assumed that the mean $g_\theta(d)$ is equal to the corrected data, $\hat{M}_{d\theta}$. In the rotated coordinate system of figure A.1, $d = x_\theta$, so the line integral can be expressed as

$$g_\theta(x_\theta) = \int_{-\infty}^{\infty} \lambda(x_\theta, y_\theta) dy_\theta, \theta \in (0, \pi), x_\theta, y_\theta, \in \Re \tag{A.2}$$

where x_θ represents transverse distance in the rotated coordinate system shown in figure A.1. We will refer to the function (and the data that it approximates) as a projection. The Fourier transform of each projection is given by

$$\begin{aligned} G_\theta(u_\theta) &= \int_{-\infty}^{\infty} g_\theta(x_\theta) e^{-j2\pi u_\theta x_\theta} dx_\theta \\ &= \int_{-\infty}^{\infty} [\int_{-\infty}^{\infty} \lambda(x_\theta, y_\theta) dy_\theta] e^{-j2\pi u_\theta x_\theta} dx_\theta \\ &= \int_{-\infty}^{\infty} \int_{-\infty}^{\infty} \lambda(x_\theta, y_\theta) e^{-j2\pi u_\theta x_\theta} dy_\theta dx_\theta \\ &= \int_{-\infty}^{\infty} \int_{-\infty}^{\infty} \lambda(x_\theta, y_\theta) e^{-j2\pi(u_\theta x_\theta + \nu_\theta y_\theta)} dy_\theta dx_\theta \mid_{\nu_\theta = 0} \\ &= \Lambda(u_\theta, \nu_\theta) \mid_{\nu_\theta = 0} \end{aligned} \tag{A.3}$$

This result, known as the projection-slice theorem, has two implications. First, the Fourier transform of a projection yields samples of the 2D Fourier transform of the image; and second, these samples lie along a line at the same angle, θ, in the frequency domain as that of the projection in the spatial domain. This result can be written in more standard notation as

$$G_\theta(\rho) = \Lambda(\rho, \gamma) \mid_{y=\theta, \rho \in \Re} \tag{A.4}$$

where the Fourier transform of the image is now expressed in polar coordinates (ρ, γ). Equation (A.3) can be used to reconstruct the image by constructing the Fourier transform in polar coordinates, interpolating to rectangular coordinates, and then taking the inverse transform.

A more efficient method can be derived as follows. The image $\lambda(x, y)$ is given by

$$\lambda(x, y) = \int_{-\infty}^{\infty} \int_{-\infty}^{\infty} \Lambda(u, \nu) e^{j2\pi(ux + \nu y)} du d\nu \tag{A.5}$$

Transforming to polar coordinates, as shown in figure A.1, using the expression $u = \rho \cos\theta$,

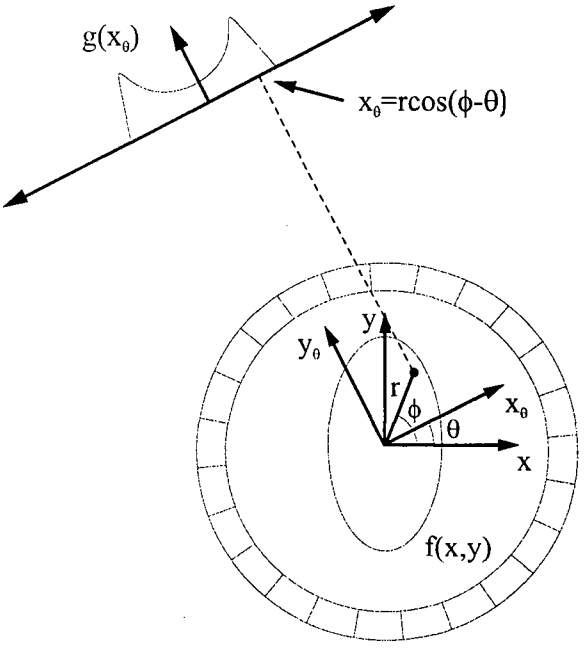

Figure A.1: Projection Geometry.

$\nu = \rho \sin\theta$, $x = r\cos\phi$, and $y = r\sin\phi$ yields

$$\lambda(r,\phi) = \int_0^{2\pi} \int_0^{\infty} \rho \Lambda(\rho\cos\theta, \rho\sin\theta) e^{j2\pi\rho r\cos(\phi-\theta)} d\rho d\theta \tag{A.6}$$

Rewriting $\Lambda(\rho\cos\theta, \rho\sin\theta)$ as $\Lambda(\rho,\theta)$ and using the facts that $\cos(\phi-\theta) = -\cos(\phi-\theta+\pi)$ and $G_\theta(\rho) = G_{\theta+\pi}(-\rho)$, this can be rewritten as

$$\lambda(r,\phi) = \int_0^{\pi} \int_{-\infty}^{\infty} \mid \rho \mid \Lambda(\rho,\theta) e^{j2\pi\rho r\cos(\phi-\theta)} d\rho d\theta \tag{A.7}$$

Applying the projection-slice theorem leads to

$$\begin{aligned} \lambda(r,\phi) &= \int_0^{\pi} \int_{-\infty}^{\infty} \mid \rho \mid G_\theta(\rho) e^{j2\pi\rho r\cos(\phi-\theta)} d\rho d\theta \\ &= \int_0^{\pi} \tilde{g}_\theta(r\cos(\phi-\theta)) d\theta \end{aligned} \tag{A.8}$$

where $\tilde{g}_\theta(x) = \mathfrak{F}^{-1}\{\mid \rho \mid G_\theta(\rho)\}$ and $\mathfrak{F}^{-1}(\cdot)$ denotes the inverse Fourier transform. Dis-

cretizing leads to the expression

$$\lambda(r,\phi) = \frac{\pi}{N_\theta} \sum_{i=0}^{N_{\theta-1}} \tilde{g}_i(r\cos(\phi - \theta_i)) \tag{A.9}$$

Equation (A.9) shows that the value of the image at a point $(r\cos\phi, r\sin\phi)$ in figure A.1 can be found by first filtering the projections with a ramp filter, then summing the filtered values at the coordinate $x_{\theta_i} = r\cos(\theta_i - \phi)$ over all projection angles θ_i. Note that the value at x_{θ_i} will contribute to all pixels along the LORs that contributed to the measurement at this point. The algorithm can be efficiently implemented by filtering each estimated projection, $g_\theta(d) = \hat{M}_{d\theta}$, with a ramp filter to yield $\tilde{g}_\theta(d)$ and then adding each filtered value into all voxels along the corresponding LOR as shown by the dashed line in figure A.1. The latter operation is called backprojection, so the algorithm is unsurprisingly called filtered-backprojection. This algorithm and its extension to three dimensions (Kinahan & Rogers (1989),Defrise et al (1989)) is used almost exclusively for image reconstruction in PET. It is identical to the algorithm used in x-ray CT except for modifications to the filter necessitated by the noise properties of PET data.

Appendix B

Scan Data

In this section each scan is presented including each of the 63 image slices, central horizontal and vertical concentration profiles, jet and depletion zone data, jet densification data, and downstream concentration profiles.

Scan	Tracer (Fraction)	Upstream Vel. (m/s)	Position of Step (Slice)	Position of Centre (X,Y)	Image Centre (Past Expansion)
1	R48	0.5	50	(68,59)	2 cm
2	R48	0.7	50	(68,59)	2 cm
3	R48	0.8	33	(60,61)	0 cm
4	R14	0.5	33	(67,62)	0 cm
5	R14	0.9	50	(66,59)	2 cm
6	R100	0.9	50	(66,59)	2 cm

Table B.1: A summary of the positional data from the scans conducted.

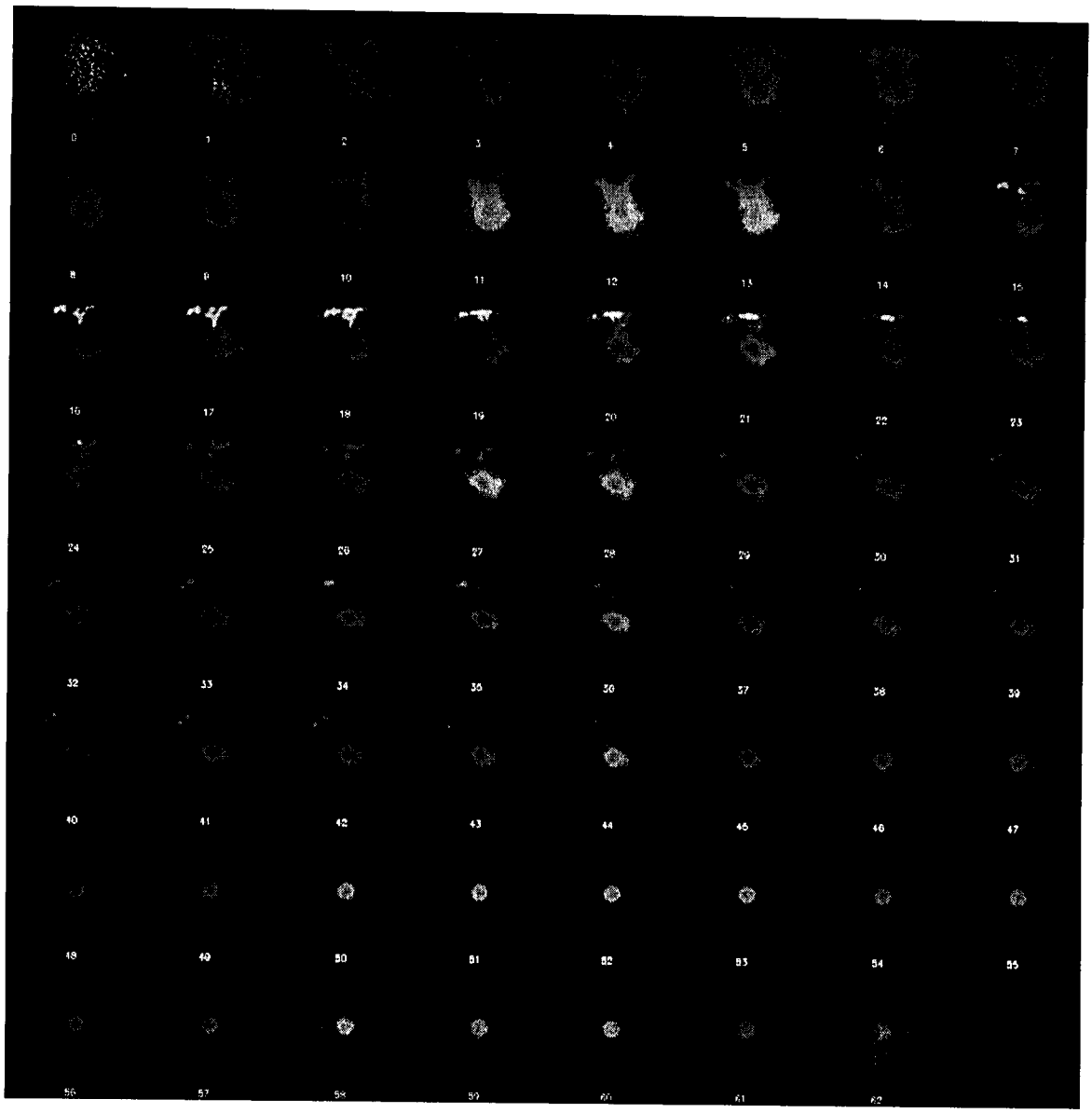

Figure B.1: Scan 1 2D Slices.

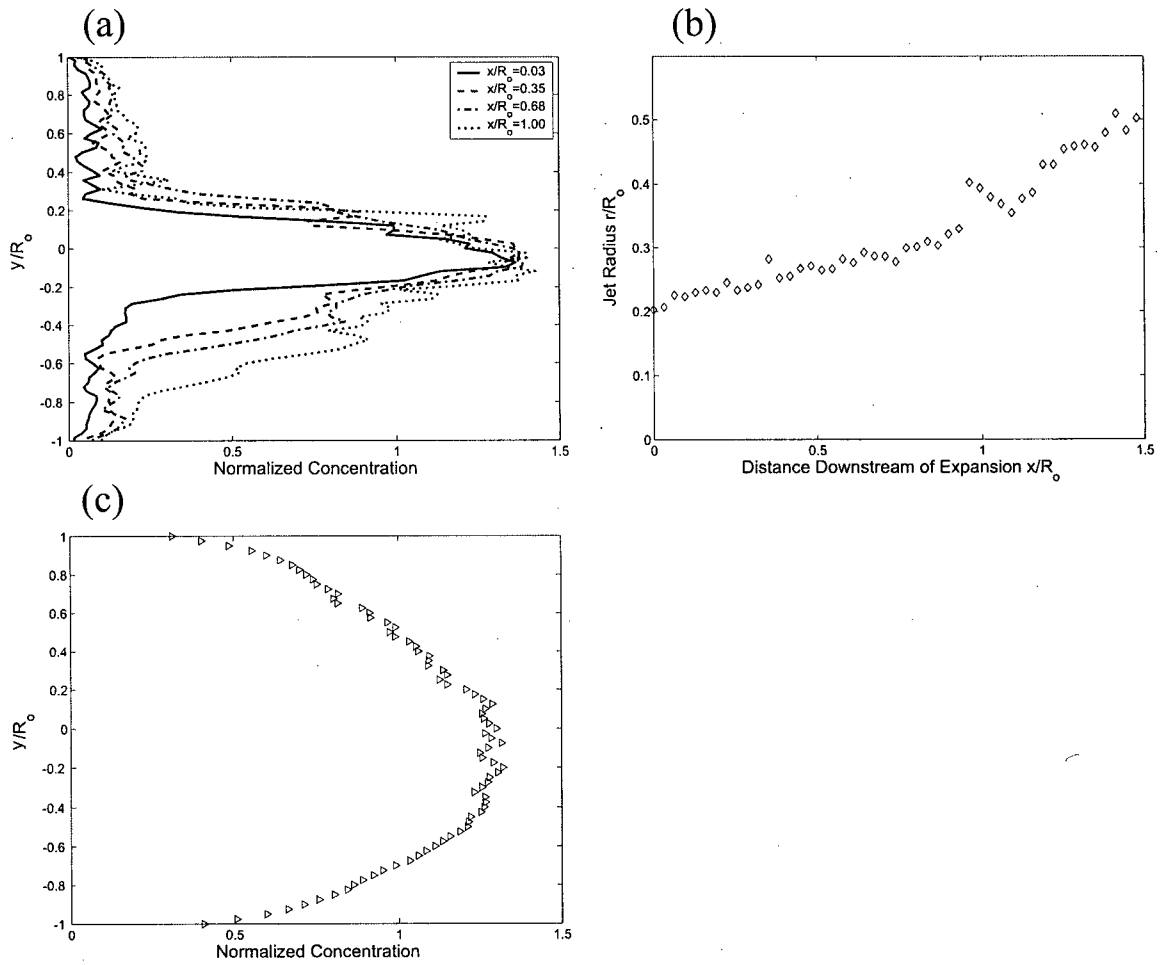

Figure B.2: Profiles for Scan 1. Horizontal Profiles (a), Jet Expansion (b), and Downstream Concentration (c).

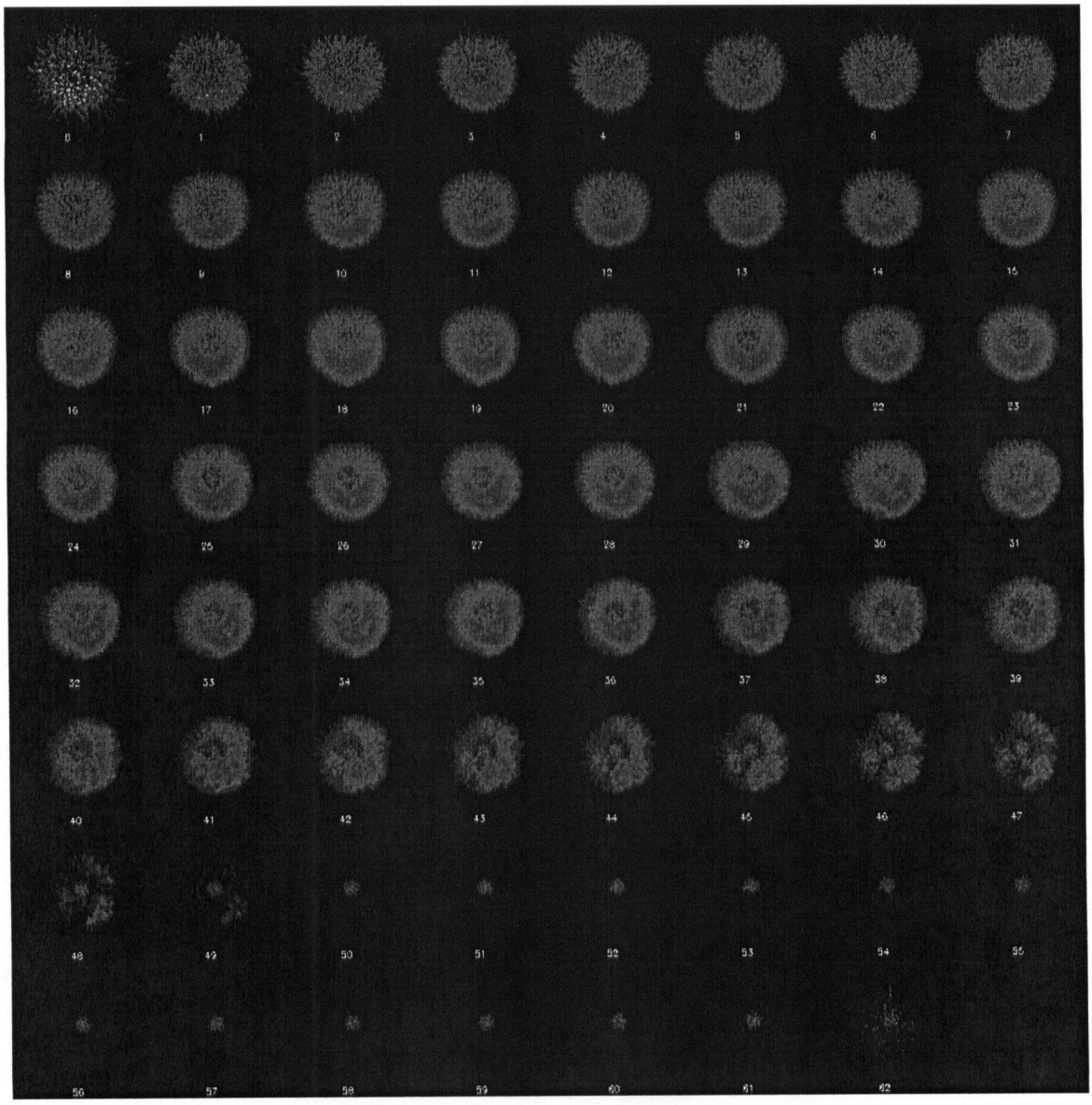

Figure B.3: Scan 2 2D Slices.

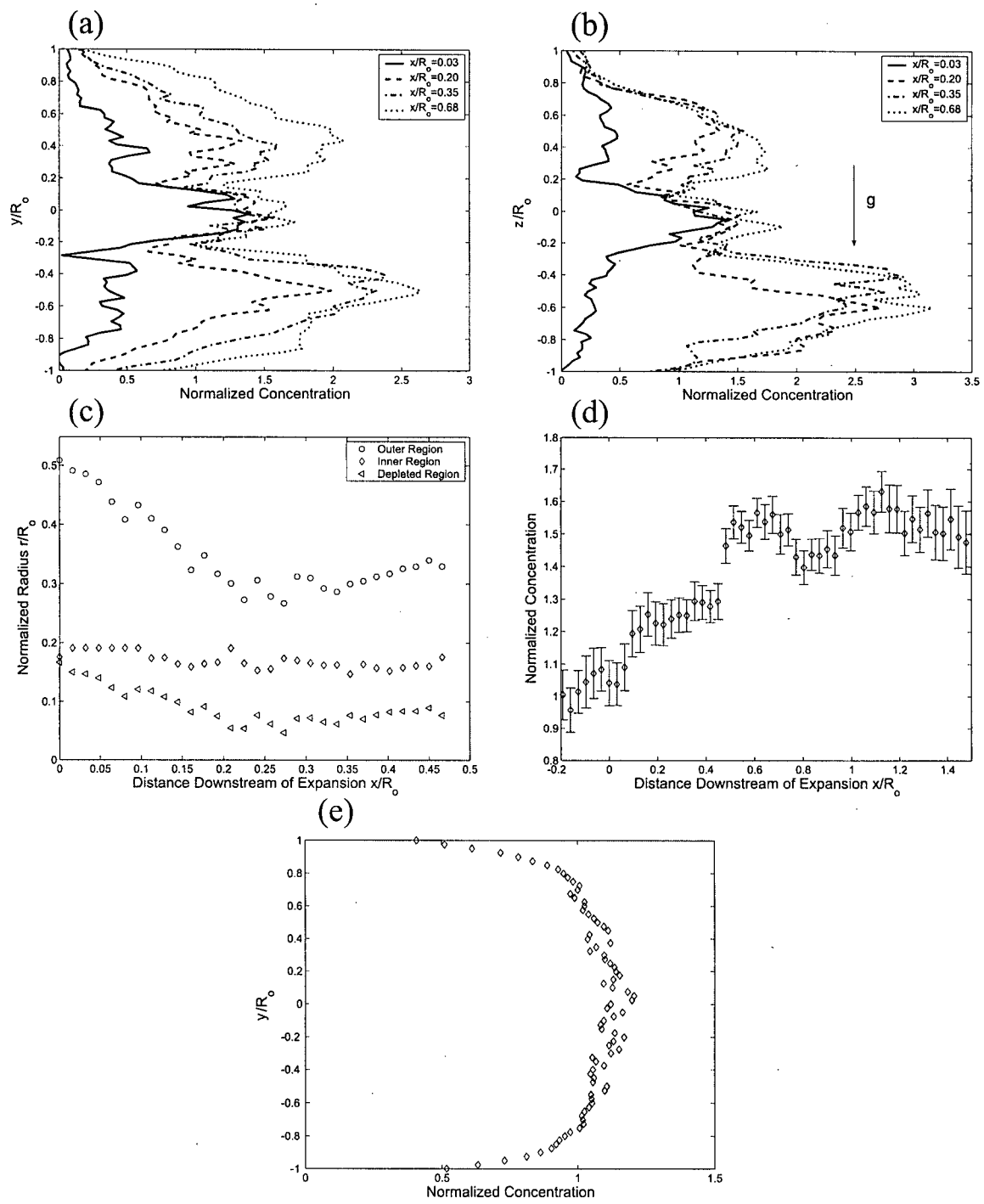

Figure B.4: Profiles for Scan 2. Horizontal Profiles (a), Vertical Profiles (b), Depletion Zone Data (c), Jet Densification (d), and Downstream Concentration (e).

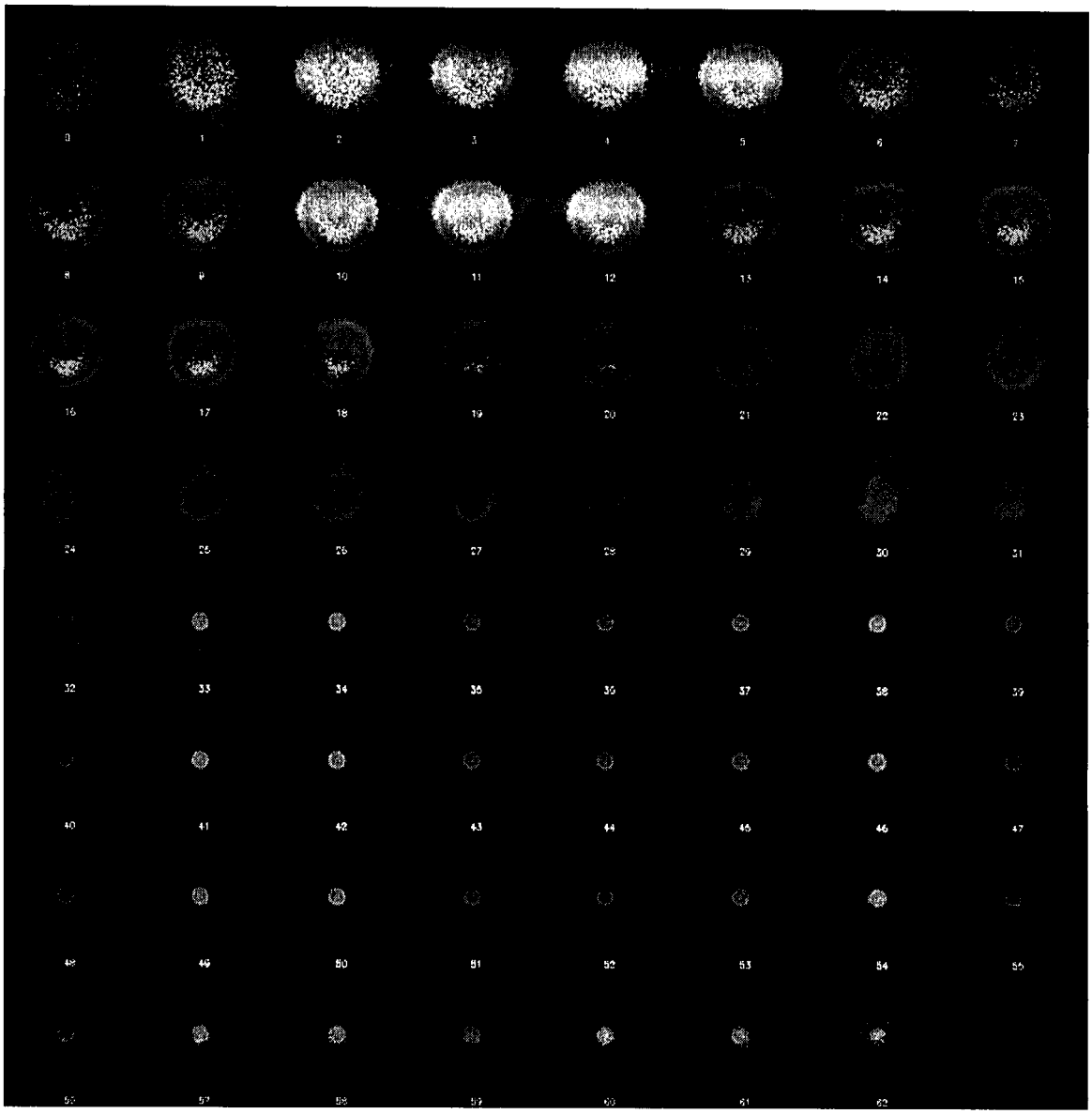

Figure B.5: Scan 3 2D Slices.

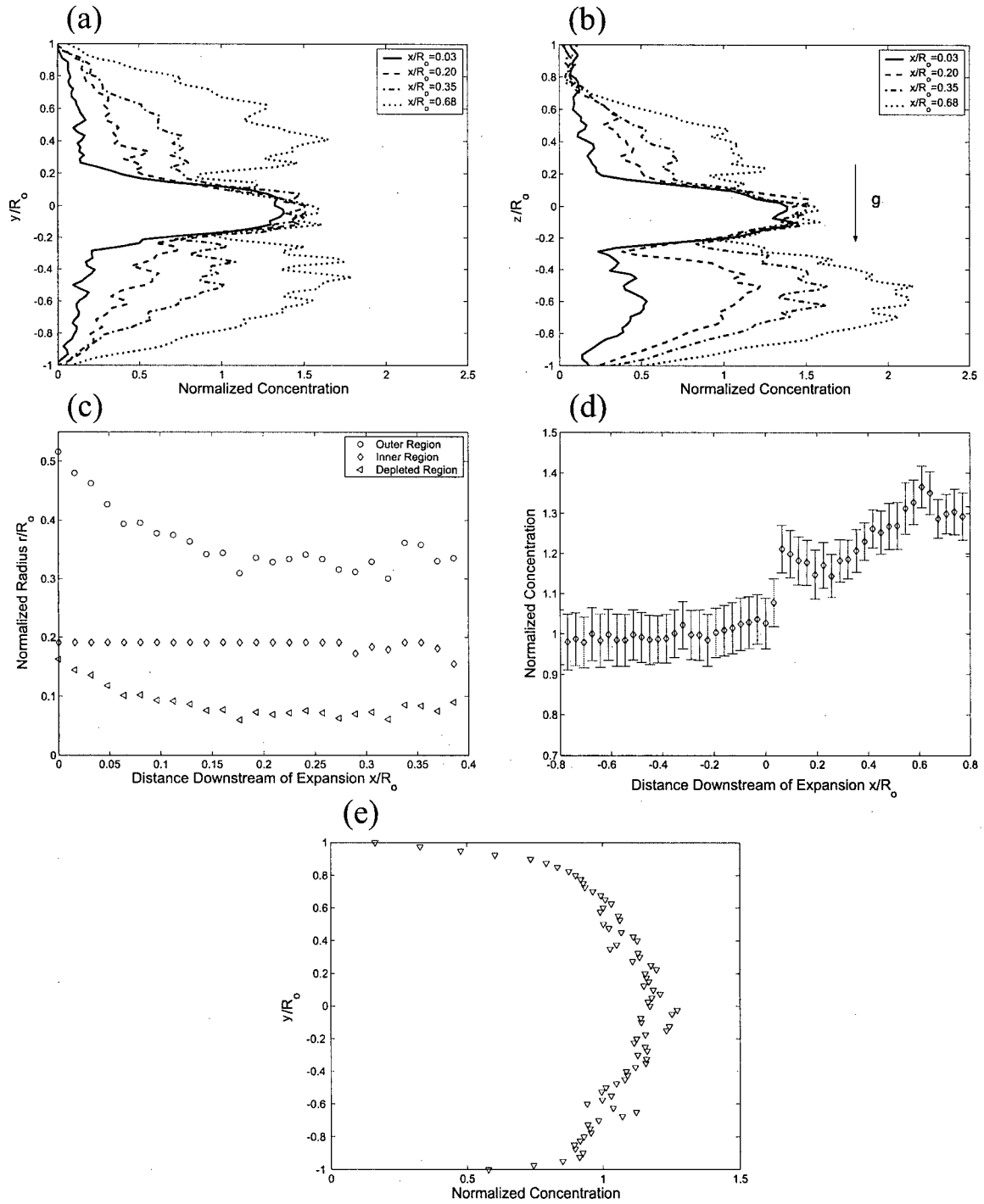

Figure B.6: Profiles for Scan 3. Horizontal Profiles (a), Vertical Profiles (b), Depletion Zone Data (c), Jet Densification (d), and Downstream Concentration (e).

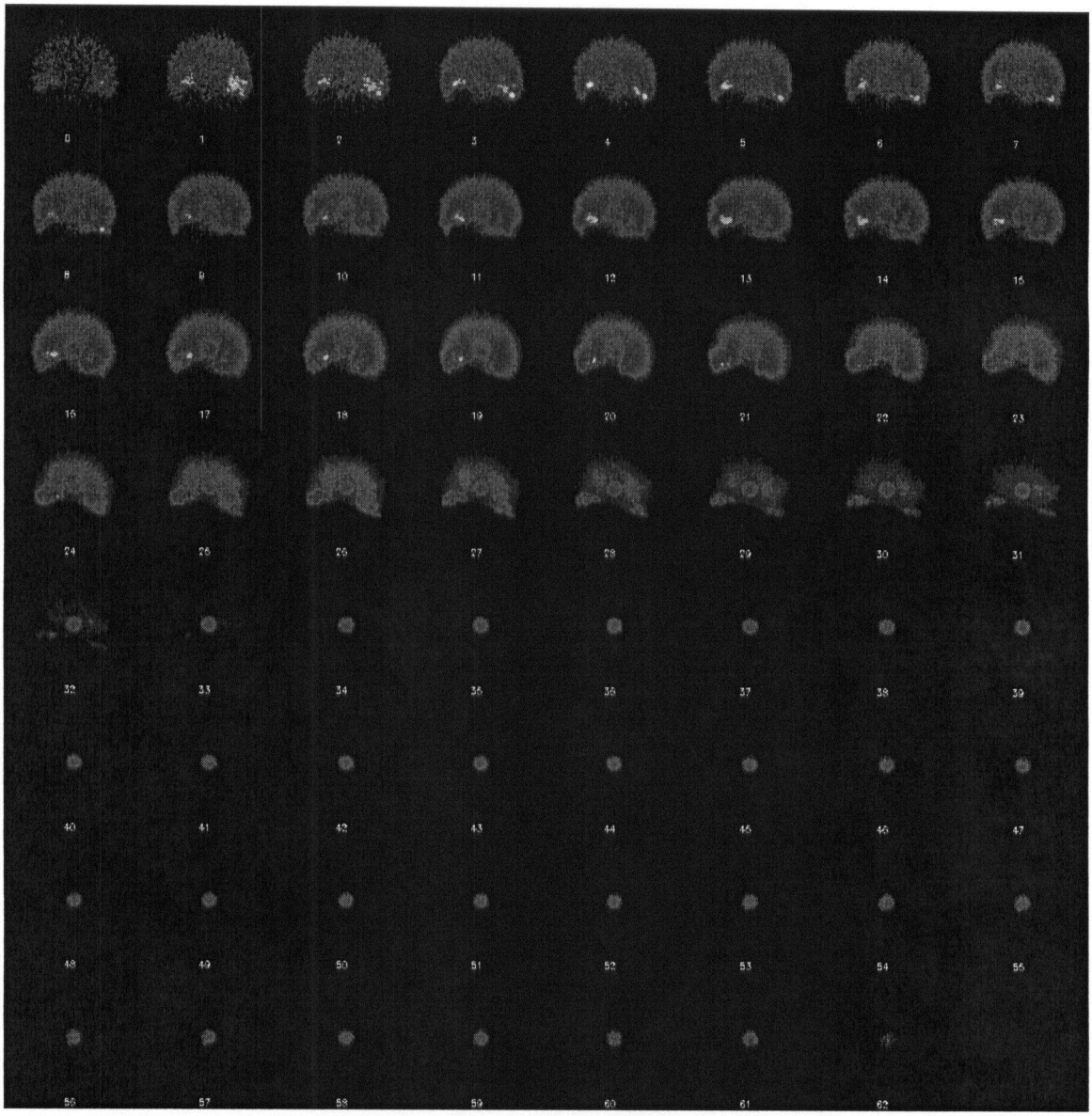

Figure B.7: Scan 4 2D Slices.

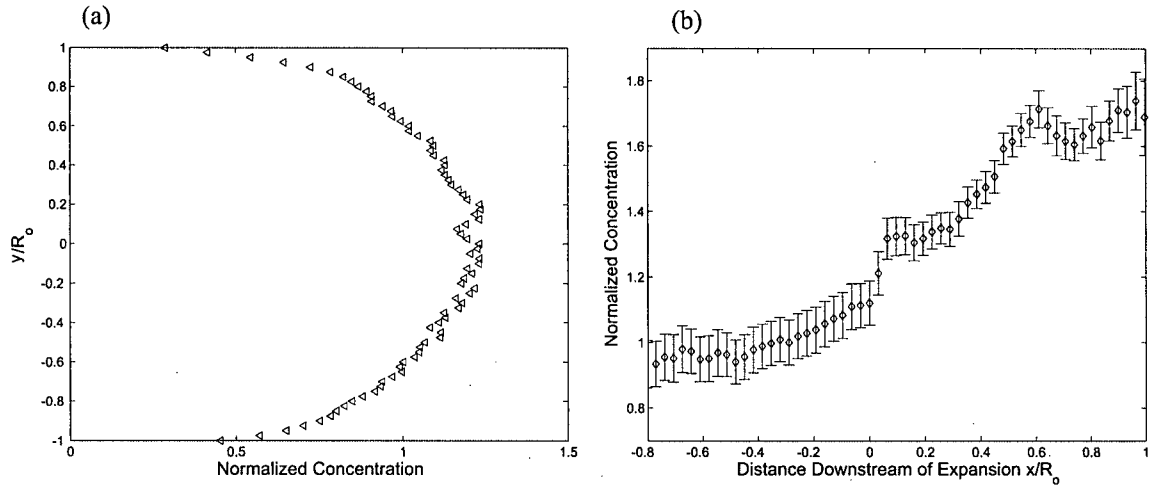

Figure B.8: Profiles for Scan 4. Downstream Concentration (a), and Jet Densification (b).

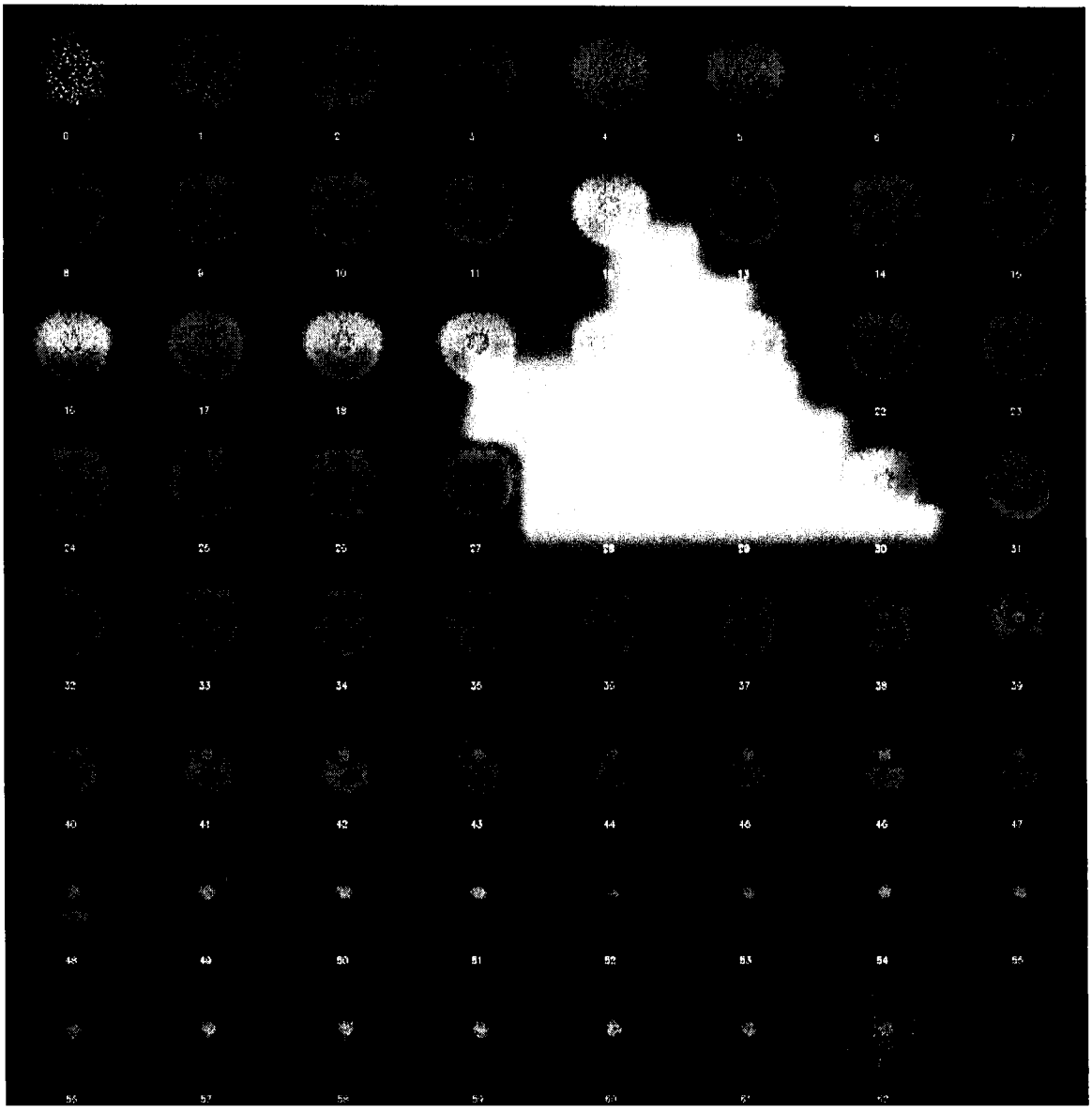

Figure B.9: Scan 5 2D Slices.

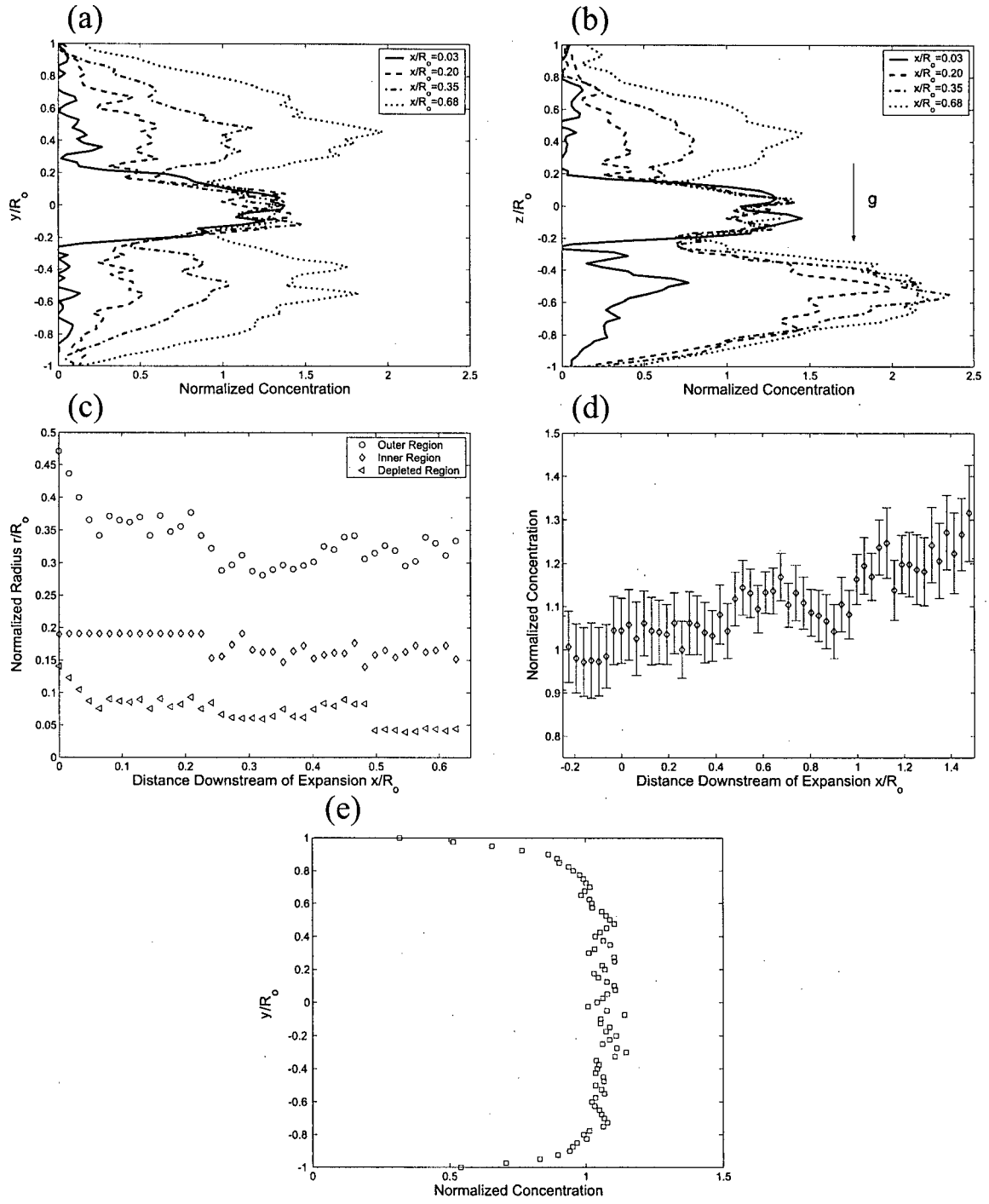

Figure B.10: Profiles for Scan 5. Horizontal Profiles (a), Vertical Profiles (b), Depletion Zone Data (c), Jet Densification (d), and Downstream Concentration (e).

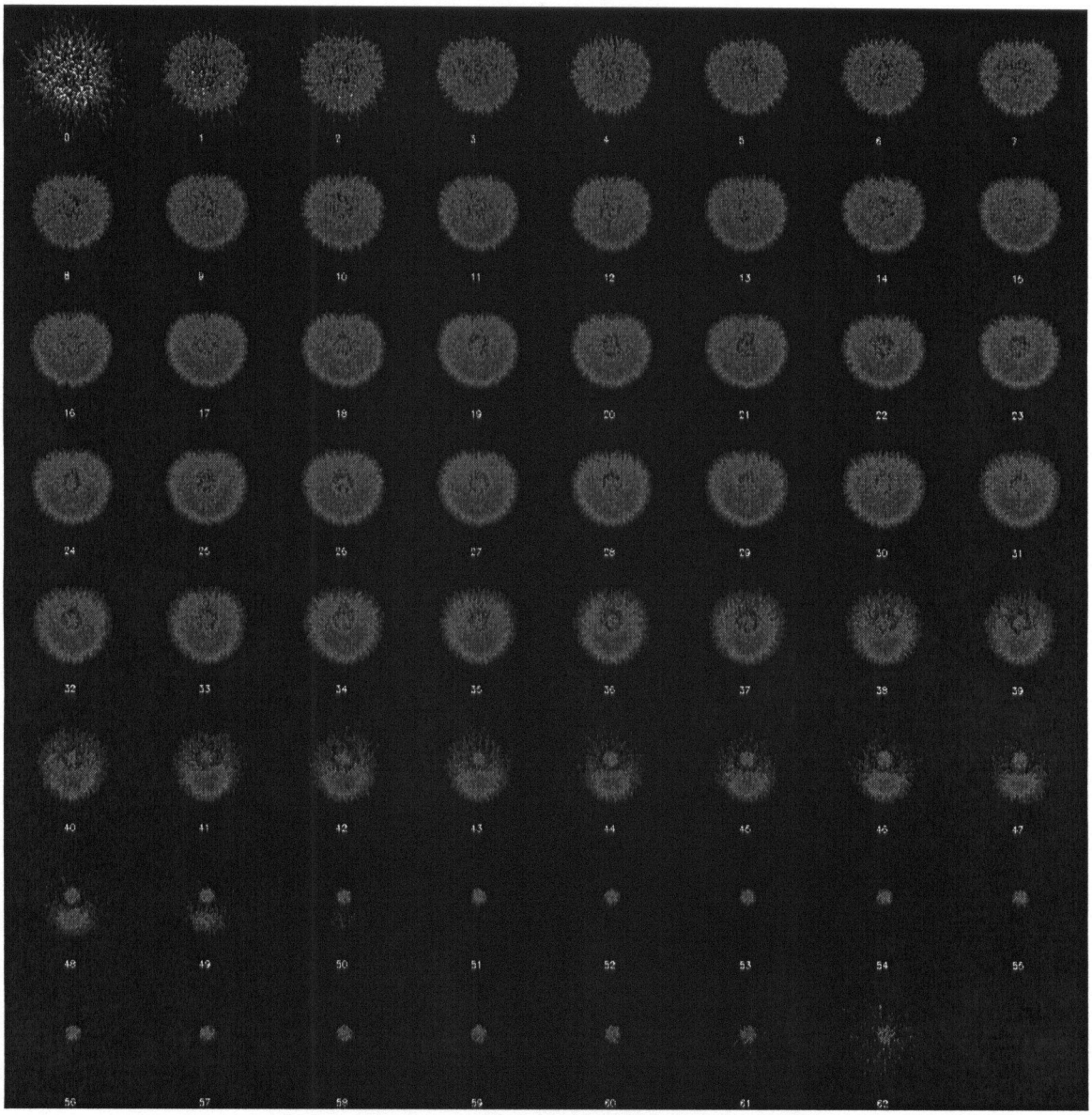

Figure B.11: Scan 6 2D Slices.

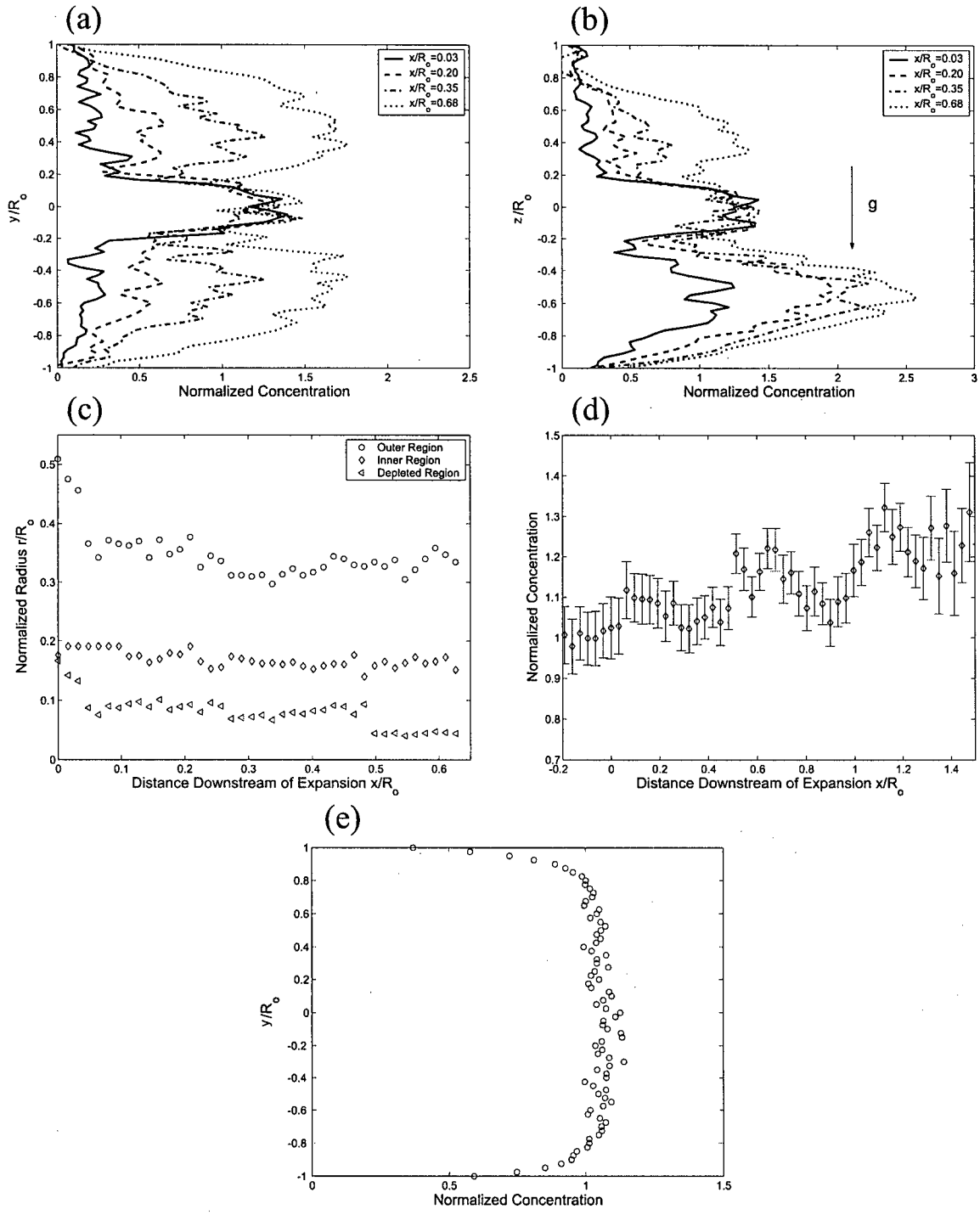

Figure B.12: Profiles for Scan 6. Horizontal Profiles (a), Vertical Profiles (b), Depletion Zone Data (c), Jet Densification (d), and Downstream Concentration (e).